** This is a non-peer reviewed preprint submitted to EarthArXiv. The manuscript has been submitted for publication in Science Advances and may be subject to change. **

Excitable Dynamics of Neoproterozoic to Early Paleozoic Atmospheric and Ocean Oxygen

Stuart Daines,[1*] Ziheng Li[2,3*]

[1]University of Exeter, Exeter, EX4 4QU, UK,
[2]Global Systems Institute, University of Exeter, Exeter, EX4 4QU, UK,
[3]State Key Laboratory of Biogeology and Environmental Geology,
China University of Geosciences, Wuhan, Hubei 430074, China

[*]Corresponding author;
E-mail: s.daines@exeter.ac.uk, zihengli@cug.edu.cn.

The geochemical carbon isotope and redox proxy record indicates that Earth's surface oxygenation involved a prolonged period of extreme variability in atmospheric and oceanic oxygen, spanning from the early Neoproterozoic to the early Paleozoic. This variability has been linked to external tectonic and evolutionary forcings, as well as to internal nonlinear feedbacks related to the redox-sensitivity of marine phosphorus burial. Here we introduce a multi-timescale dynamical systems framework to examine the stability of the coupled biogeochemical cycles of phosphorus, carbon, and oxygen. Our analysis reveals the criteria for system stability, and identifies an "excitable" regime where small forcings can trigger ocean oxygenation and anoxic events. We suggest that transitions through stable, excitable and oscillatory regimes can explain the Neoproterozoic to Paleozoic geochemical record, and that dynamical constraints at the Earth system level account for more of these patterns

and trends than has been previously recognized.

Introduction

The geochemical record demonstrates that the rise of atmospheric and ocean oxygen from low Proterozoic levels, with oxygen at $\approx 1 - 10\%$ present atmospheric level (PAL) and predominantly anoxic oceans, to modern Phanerozoic levels occurred over a protracted interval, from the early Neoproterozoic (at $\approx$ 900 Ma) to the early Paleozoic. Basin-scale sulfate evaporite deposition in the Tonian ($\approx$ 850 Ma) (*1, 2*) with low $\delta^{34}\mathrm{S} \approx 16‰$ indicate at least transiently oxygenated seawater with relatively high sulfate concentrations. An increase in the abundance of sedimentary charcoal (*3*) indicates a Paleozoic Oxygenation Event at 450 - 400 Ma where atmospheric oxygen rose to $>$ 65% PAL and thereafter remained at near-modern levels, whilst the cerium isotope record (*4*) suggests that modern levels of ocean oxygenation were not reached until the Devonian. However, during this interval from the Neoproterozoic to early Paleozoic, although there are no strong constraints from geochemical proxies, isotope mass balance models indicate that atmospheric oxygen was highly variable in the range 1 - 50 % PAL (*5*). Other geochemical proxies reveal that ocean oxygen was also variable, with an overall secular trend from ocean oxygenation events (OOE) in an early Neoproterozoic anoxic background to anoxic events (OAE) against a more oxic later Cambrian background state, Fig. 1.

Multiple OOEs are seen in a predominantly anoxic Neoproterozoic to early Cambrian oceans (*6–10*), with globally correlated events including the aftermath of the Sturtian (717 - 659 Ma) (*8*), Marinoan ($\approx$ 640 - 635.5 Ma) and Gaskiers (582 Ma) glaciations, and the Shuram ($\approx$ 574 Ma) (*11*) and BACE ($\approx$ 540 Ma) (*10*) negative carbon isotope events. The early Cambrian then shows more complex and rapid variability in ocean oxygen (*10, 12*), followed by apparent oscillations with a periodicity of 3 - 4 My from 524 - 514 Ma (*13*). The end-Cambrian SPICE event (499 Ma) (*14*) is the first unambiguous isolated OAE (*15*), with the Hirnantian OAE (444

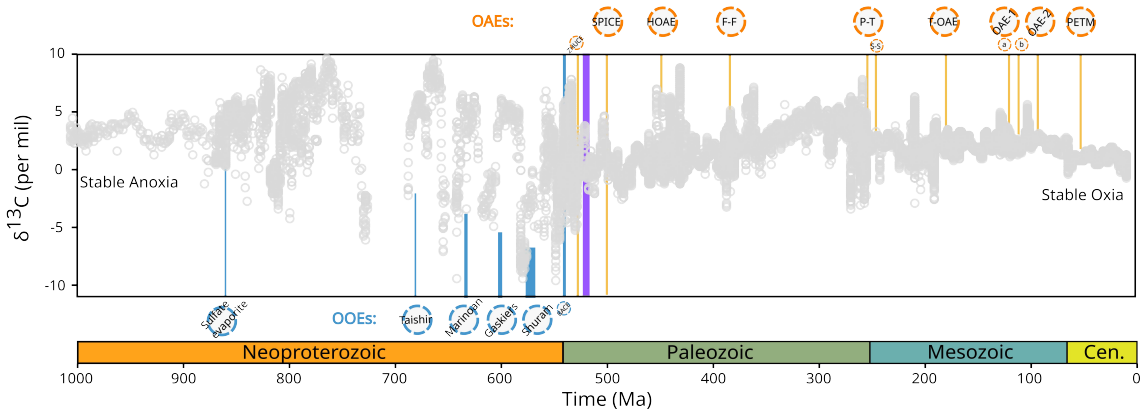

Fig. 1. Compilation of carbon isotope record of the last 1 billion years with geochemically identified OOEs and OAEs. δ^{13}C compilation 1000-700 Ma from (*21*), 700-0 Ma from (*18*). OOE (blue bars): sulfate evaporite deposition ($\approx$ 850 Ma) (*1, 2*), Taishir (aftermath of the Sturtian) (717 - 659 Ma) (*8*), Marinoan ($\approx$ 640 - 635.5 Ma) and Gaskiers (582 Ma) glaciations, Shuram ($\approx$ 574 Ma) (*7,11*), BACE ($\approx$ 540 Ma) (*7,10*). OAE (orange bars): ZHUCE ($\approx$ 526 Ma) (*12*), later Phanerozoic OAEs (*15*). Redox state oscillations with a 3 - 4 My periodicity from 524 - 514 Ma (*13*) are shown as a purple bar. Not shown due to ambiguities in stratigraphy (*19*): an additional proposed OOE (*7*) and OAE (*14*) between BACE and ZHUCE. See Supplementary Materials Fig S1 for selected intervals with expanded scales.

Ma) (*16, 17*) coincident with end-Ordovician mass extinction, and isolated OAE continuing through the Phanerozoic (*15*) with considerable diversity and a secular trend towards shorter and rarer events. All of these events show a characteristic carbon isotope signature (*18, 19*) (Fig. 1, Supplementary Materials Fig. S1), with positive excursions in δ^{13}C consistent with enhanced organic carbon burial during episodes of marine anoxia (OAE), and negative excursions consistent with a reduction during OOE. Consistent with these trends, the variability in the carbon isotope record also shows a secular trend with a Neoproterozoic maximum in variability and a decrease through the Phanerozoic (*20*).

Although the two-way feedbacks between biological evolution and oxygen remain a matter for debate, it is likely that stability, as well as overall oxygen level, is important as a control on biotic evolution. Ocean redox state is clearly both a major control on the ecological success of benthic metazoan ecosystems (*22*) and a major driver of marine extinctions (*11, 23*). Spatial

and temporal variability may also have been a driver of early metazoan diversification from the Ediacaran through the Cambrian (*24, 25*). Conversely, evolutionary innovations in the water column and sediment (*26–29*) will have modified both water column oxygen demand and the efficiency of carbon and phosphorus burial, creating and modifying feedbacks from the biota to the ocean environment.

The overall rise of atmospheric oxygen over Earth history reflects a combination of an increase in the oxygen source due to organic carbon burial and a decrease in sinks (*30*). The most parsimonious explanation is that since the early Paleoproterozoic oxygenation of the atmosphere, the major control is organic carbon burial controlled by phosphorus as the ultimate limiting nutrient, with the rise in oxygen then due to a combination of a secular increase in the global organic carbon to phosphorus burial ratio and an increase in phosphorus supply from weathering (*31–33*), primarily due to macroevolutionary innovations in the marine and then the land biota (*26, 28, 34*). The feedback control on atmospheric oxygen then changed from a Proterozoic regime with anoxic oceans and atmospheric oxygen weakly regulated by the oxygen sensitivity of oxidative weathering (*32*), through an apparently unstable Neoproterozoic - early Paleozoic regime (*31*), to a stable later Phanerozoic regime with atmospheric oxygen maintained at near-modern levels by feedback due to the fire-sensitivity of the terrestrial biota (*35, 36*).

The Neoproterozoic - early Paleozoic variability of atmospheric and ocean oxygen on timescales $\leq 10^7\,\mathrm{yr}$ must reflect some combination of external (tectonic or evolutionary) forcing and the internal feedbacks. A fundamental non-linearity and coupling between oxygen, carbon, and marine phosphorus is introduced by the marine redox and phosphorous dependence of marine phosphorus burial (*37, 38*). Using models for the coupled oxygen and marine phosphorus cycles that include this effect, Handoh & Lenton (*39*) proposed that sequences of Phanerozoic OAEs could be generated by self-sustaining coupled oscillations between the phosphorous and atmospheric oxygen reservoirs. Alcott *et al.* (*31*) showed that the progressive oxygenation over Earth

history results in a potentially unstable regime during the Neoproterozoic-Cambrian transition from anoxic to oxic oceans. Using a model for the coupled marine phosphorus and ocean-atmosphere carbon cycles, Bachan *et al.* (*20*) proposed that the redox dependence of marine C:P burial ratio could explain the characteristic 0.5 - 10 My timescale of Phanerozoic $\delta^{13}\mathrm{C}$ excursions and their secular trend. However, an overall understanding of the controls on stability and dynamics has been lacking, that accounts for the potential role of both (i) external forcings and intrinsic amplifying feedbacks and possible instability, and (ii) that can disentangle the contributions of local process controls and system-level feedbacks to the coupled system response (*40*).

The biogeochemical cycles of oxygen, phosphorus and carbon as a multi-timescale dynamical system

Well-mixed global Earth surface biogeochemical reservoirs comprise a dynamical system, with reservoir content evolving with time in response to globally-integrated fluxes. As the reservoir timescales are short compared to the geological record, the corresponding reservoir content must be regulated by feedback on either sources or sinks (Fig. 2), with the primary feedbacks including the silicate weathering thermostat for carbon (*41*), the weathering source and burial sink for marine phosphorus (*42*), and (prior to land plant evolution) marine organic carbon burial and oxidative weathering (*32*) for oxygen. The system level feedback structure and stability can be analysed mathematically as a property of the dynamical system itself, and abstracted away from the specific processes involved (even if those are intentionally fictional as in the case of the "Daisyworld" parable (*43*)). However, models of long-timescale Earth system biogeochemistry (*e.g.* (*33, 44*)) have remained implicitly within a conceptual and mathematical framework of steady-states and feedbacks which cannot represent variability in the observed record (*45, 46*). Although possible limit-cycle oscillations have been previously iden-

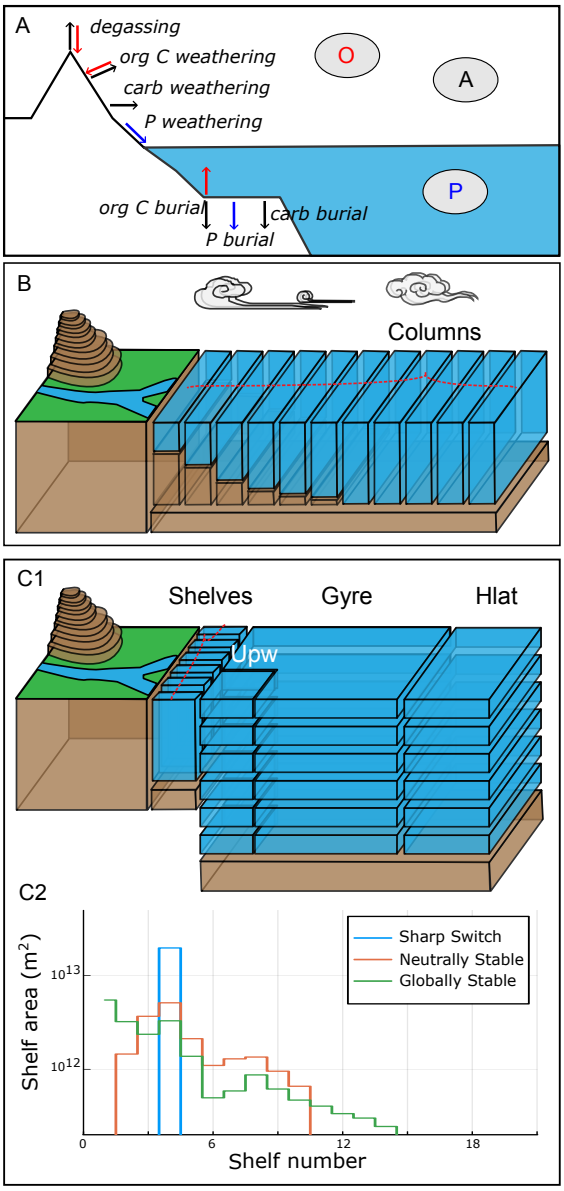

Fig. 2. Model schematics. (**A**) Global model for coupled biogeochemical cycles of marine phosphorus P and atmosphere-ocean carbon A and oxygen O. Arrows indicate interaction between weathering, degassing, and burial processes and Earth atmosphere-ocean inventories. (**B**) Idealized ocean column model for spatial heterogeneity of ocean organic carbon and phosphorus burial. (**C1**) Intermediate complexity ocean box model with two ocean columns and multiple shelf environments; (**C2**) shelf-area distribution adjusted to approximate the three idealised distributions of marine burial fluxes across oceanfloor redox environments shown in Fig. 3 (shelf nutrient level increases and shelf oxygen decreases with increasing shelf index), see Supplementary Materials Fig. S4 for details.

tified within the coupled phosphorus-oxygen biogeochemical cycles (*31, 39*), the broader implications of such an unstable regime can only be revealed by a global phase-space view of system dynamics that makes it possible to identify stable and unstable regimes of a nonlinear system, including boundaries of locally-stable regions and possible excitability (*45, 47, 48*), response to stochastic forcings (*49, 50*), and sensitivity to the rate at which forcings change (*46, 51, 52*).

We argue here that explicit consideration of timescale separation is the key step that is required to apply dynamical systems theory consistently to global biogeochemical cycles. Firstly, timescale separation is the fundamental organizing principle that can be used to define a hierarchy of models for the coupled Earth system and enable representation of the global biogeochemical dynamics as a low dimensional system. A general property of multi-time-scale dissipative dynamical systems (*53–55*) is that the state space of a high-dimensional system decomposes into a combination of a high dimensional space of fast variables (*e.g.* the atmosphere adjustment timescale $\sim 10\,\mathrm{yr}$, or the per-cell tracer concentration and circulation in an ocean model, timescale $\sim 10^3\,\mathrm{yr}$) and a low-dimensional slow manifold (*e.g.* the global marine phosphorus inventory and atmosphere-ocean oxygen and carbon, timescale $\sim 10^5 - 10^7\,\mathrm{yr}$), with the fast variables rapidly reaching a quasi-steady state, and system evolution then described by evolution on the slow manifold (*56, 57*) combined with stochastic fluctuations due to unresolved fluctuations on the fast timescales. This property can be exploited to represent the long-timescale Earth system biogeochemical dynamics, calculating the changes in global atmosphere-ocean oxygen, carbon and marine total phosphorus inventories due to global integrals of spatially and temporarily averaged biogeochemical fluxes.

Once reduced in this way to a low-dimensional system, timescale separation between the remaining global variables can then further exploited to understand the global structure of the phase space. An illustrative example is the "nitrostat" (*42*) in the modern global ocean: nitrate adjusts on an ocean circulation timescale of $\sim 10^3\,\mathrm{yr}$ in response to longer timescale evolution

of marine phosphorus and oxygen. This illustrates the essential ingredients for a consistent understanding of Earth system biogeochemical dynamics: the fast variables in the system are "slaved" to the slow variables, and the adjustment process following a displacement from equilibrium consists of an initial fast evolution followed by a slow drift within a lower-dimensional slow manifold. The timescales for the Earth surface reservoirs considered here can be estimated as the ratio of typical Neoproterozoic reservoir content (mol) to flux ($\mathrm{mol\,yr^{-1}}$) (Supplementary Materials Table *S2*): phosphorus P $\tau_P \approx 3 \times 10^{15}/4 \times 10^{10} \approx 10^5\,\mathrm{yr}$; atmosphere-ocean carbon A $\tau_A \approx \sqrt{(10)} \times 3 \times 10^{18}/7.9 \times 10^{12} \approx 10^6\,\mathrm{yr}$ (assuming $p\mathrm{CO}_2 \approx 10\times$ modern value); and oxygen O $\tau_O \approx 0.5 \times 3.7 \times 10^{19}/4.5 \times 10^{12} \approx 4 \times 10^6\,\mathrm{yr}$ (assuming 0.5 PAL). Given this wide range of timescales, it is therefore misleading to try and define a system of feedbacks relative to a steady-state (*e.g.* (*36*)), and the system response to forcings may in fact be sensitive to the rate at which forcings change relative to the various internal timescales that control the rate at which the system responds (*40, 45, 51, 52*).

A dynamical systems approach to problems with a clear separation of time scales can be formalized mathematically using the techniques of geometric singular perturbation theory (GSPT) (*56–58*). We show an overview of the mathematical approach for a system of ordinary differential equations (ODEs) with two different timescales in the Supplementary Materials, but prioritize here the qualitative global insights obtained using numerical models. The key principle is to decompose the system dynamics into fast and slow segments in phase space. Potential instability (resulting in limit cycle oscillations or excitability) is then identified by the presence of "folds" in the slow manifold where the fast variable nullcline changes from "attracting" to "repelling". Stability boundaries are defined by the locations of the folds and repelling segments; crossing a stability boundary then leads to fast-timescale jump to another part of the slow manifold.

Here we employ this geometrical approach to dynamical systems, coupled with a hierarchy

of models (Fig. 2), to decipher the factors influencing the interconnected dynamics of oxygen, phosphorus, and carbon cycles and to identify how secular evolution through different regimes explains the patterns in the variability of the Neoproterozoic to Paleozoic record. We first use a minimal two-dimensional phosphorus-oxygen model to derive the criteria for global stability, and show how this is linked to the local redox sensitivity of phosphorus burial. We then generalize the model to include the carbon cycle and land-surface weathering feedbacks, and show that whilst the boundaries of globally stable and unstable regimes are qualitatively unchanged, faster phosphorus-carbon controlled events and limit cycles may occur. We show that secular trends in the periodic variability of ocean oxygen are generic properties of the system dynamics, and that a further generic feature of the phase plane geometry is the existence of marginally (un)stable excitable regimes. We show that combining slow secular evolution with small stochastic forcing predicts evolution through regimes with both randomly spaced and quasiperiodic OOE and OAE events. Finally we discuss the limitations of our approach and implications for future work.

Results

Globally averaged marine phosphorus burial may be a non-monotonic function of phosphorus level

The long-timescale Earth system biogeochemical dynamics of marine phosphorus P (Eq. 1), atmosphere-ocean oxygen O (Eq. 2), and carbon A (Eq. 3)) depends on the global marine burial fluxes of phosphorus $F_{P\_b}(O, P)$ and organic carbon $F_{Corg\_b}(O, P)$. Many previous long-timescale biogeochemical models (*31, 33, 37, 38, 59*) have employed zero or low-dimensional box models to represent the marine environment, which necessarily then requires a parameterisation of global marine burial fluxes that combines spatial averaging and local controls. Here we make this explicit by first considering local controls, and then employ a hierarchy of two

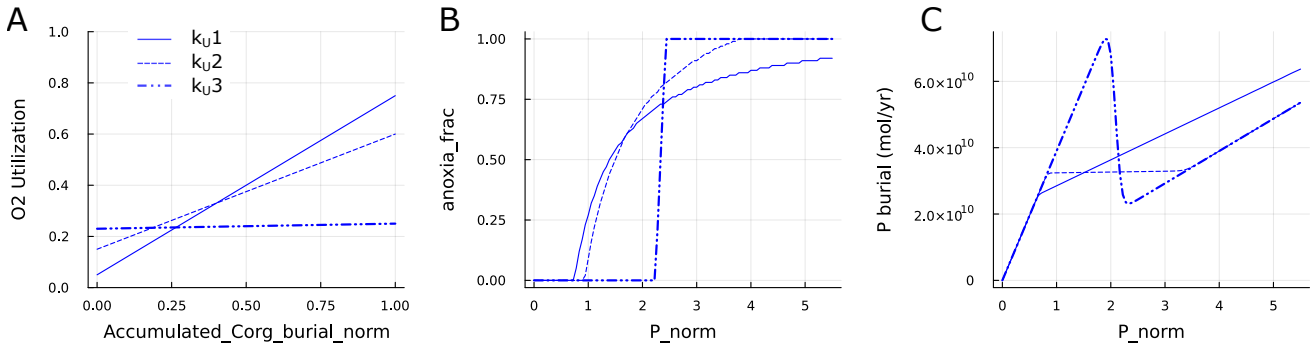

Fig. 3. Local redox dependence combines with globally averaged oceanfloor oxygen to determine global marine phosphorus burial. (**A**) Parameterisations of oceanfloor oxygen demand k_U as a function of normalized global cumulative organic carbon burial C_{org_cuml} in an idealized column model. Solid line (k_U1) shows the effect of a global distribution of marine burial over a broad range of oceanfloor redox environments, dash-dot line (k_U3) a narrow range, dotted line (k_U2) an intermediate case. (**B**) Fraction of global marine organic carbon burial under anoxic conditions as a function of normalized marine phosphorus at constant atmospheric oxygen of 0.5 PAL, for the three parameterisations of k_U shown in panel **A**. (**C**) Global marine phosphorus burial as a function of normalized marine phosphorus at constant atmospheric oxygen of 0.5 PAL, illustrating non-monotonic behaviour for case k_U3 with all global marine burial in a narrow range of redox conditions.

ocean models to perform a spatial averaging over ocean floor environments: a column-based model for oceanfloor oxygen and burial flux, and an intermediate-complexity ocean model.

Empirically, in modern marine environments the local organic carbon to organic matter associated phosphorus (Corg:Porg) sediment burial ratio is found to be oxygen sensitive, with typical molar Corg:Porg burial ratios of $\approx$ 200 in oxic environments and as high as $\approx$ 4000 in anoxic environments (*37, 60*). The overall ratio of organic carbon to total phosphorus burial (Corg:Ptotal, including all phosphorus fractions: organic matter associated, carbonate fluorapatite and iron-sorbed) varies by at least a factor of two, from $\approx$ 50 in oxic environments to $\approx$ 200 in anoxic environments (*61*). Plausibly, the major controls are the redox-dependent availability of iron oxides (*62*), and bacterial phosphate metabolism (*63*) under fluctuating redox conditions, with recent suggestions that calcium concentration may also play a role (*64*), and "sink switching" during early diagenesis complicating the interpretation. Although the actual oxygen

dependence is poorly constrained, it is consistent with the majority of the change in Corg:Ptotal occurring within a limited range of oxygen concentration $< 20\mu\mathrm{M}$ (Figure 2 in (*61*)).

The local redox dependence of the Corg:Ptotal burial ratio then introduces two competing effects on globally-integrated marine phosphorus burial: increasing productivity tends to drive an increase in phosphorus burial with increasing marine phosphorus, but also tends to create marine anoxia which reduces phosphorus burial. We use a minimal marine ecosystem model to calculate spatially integrated burial fluxes including these effects. We assume that export production and ocean floor fluxes are proportional to marine phosphorus, with burial fluxes defined by a burial factor. Organic carbon burial is assumed to be independent of oxygen, hence global marine organic carbon burial is linearly proportional to marine phosphorus, whilst phosphorus burial includes (local) oceanfloor oxygen dependence assumed to be a step transition at zero oxygen.

Results using the idealized column model (Fig. 3) demonstrate how the balance between these competing processes depends on the spatial distribution of marine burial fluxes across a heterogeneous ocean floor environment, represented by parameterisations of oceanfloor oxygen demand k_U as a function of normalized cumulative organic carbon burial C_{org_cumul} (see Materials and Methods). If burial fluxes are distributed over a wide range of oceanfloor redox conditions (case $k_U 1$, solid line in Fig. 3), the fraction of global marine organic carbon burial in anoxic oceanfloor environments increases only gradually with increasing marine phosphorus level, the effect of increasing productivity on burial flux dominates, and global marine phosphorus burial is a monotonically increasing function of marine phosphorus. Conversely, if marine burial fluxes are distributed among environments with homogeneous oceanfloor redox conditions (case $k_U 3$, dash-dot line in Fig. 3), then all local burial environments become anoxic at a threshold marine phosphorus level, resulting in a reduction in marine phosphorus burial and a non-monotonic behaviour of globally-integrated phosphorus burial as a function of

marine phosphorus. Sensitivity studies (Supplementary Materials Fig. S12) show how assuming a gradual dependence of local phosphorus burial on local oceanfloor oxygen has a similar effect on globally-integrated phosphorus burial to that of distributing burial among a range of redox environments. Results using the intermediate-complexity ocean model show how the distribution of marine burial fluxes among different redox environments can be related to the distribution of shelf areas across a catalog of ocean shelf environments with different ocean connectivity and hence nutrient levels (Fig. 2 *C*, Supplementary Materials Fig. S4).

Nullclines define stable and oscillatory regimes of the P-O dynamical system

To introduce the dynamical systems approach and to compare to previous model results (*31, 39, 65*), we consider initially a phosphorus-oxygen only model with constant phosphorus weathering input. This can be analysed as a fast-slow dynamical system, with a short $\approx 10^5\,\mathrm{yr}$ phosphorus timescale, and a long $10^6 - 10^7\,\mathrm{yr}$ oxygen timescale. The overall stability and approximate time evolution of the system can then be deduced from the location and properties of the oxygen (dO/dt=0) and phosphorus (dP/dt=0) nullclines. Following the approach of GSPT ((*56, 57*), see Supplementary Materials), this can approximated by the evolution in the singular limit of complete timescale separation, where trajectories consist of fast jumps in phosphorus at constant oxygen, and slow evolution along the phosphorus nullcline (the *critical manifold*), Fig. 4.

The location of the critical manifold is determined by the balance between phosphorus input from weathering (assumed constant here) and marine phosphorus burial. We show in Fig. 4 the three critical manifolds corresponding to the idealized column model configurations from Fig. 3. The limiting behaviours at high or low oxygen (where the ocean floor is fully oxic or anoxic) correspond to vertical lines in the P-O phase plane, with Corg:Ptotal burial ratio fixed

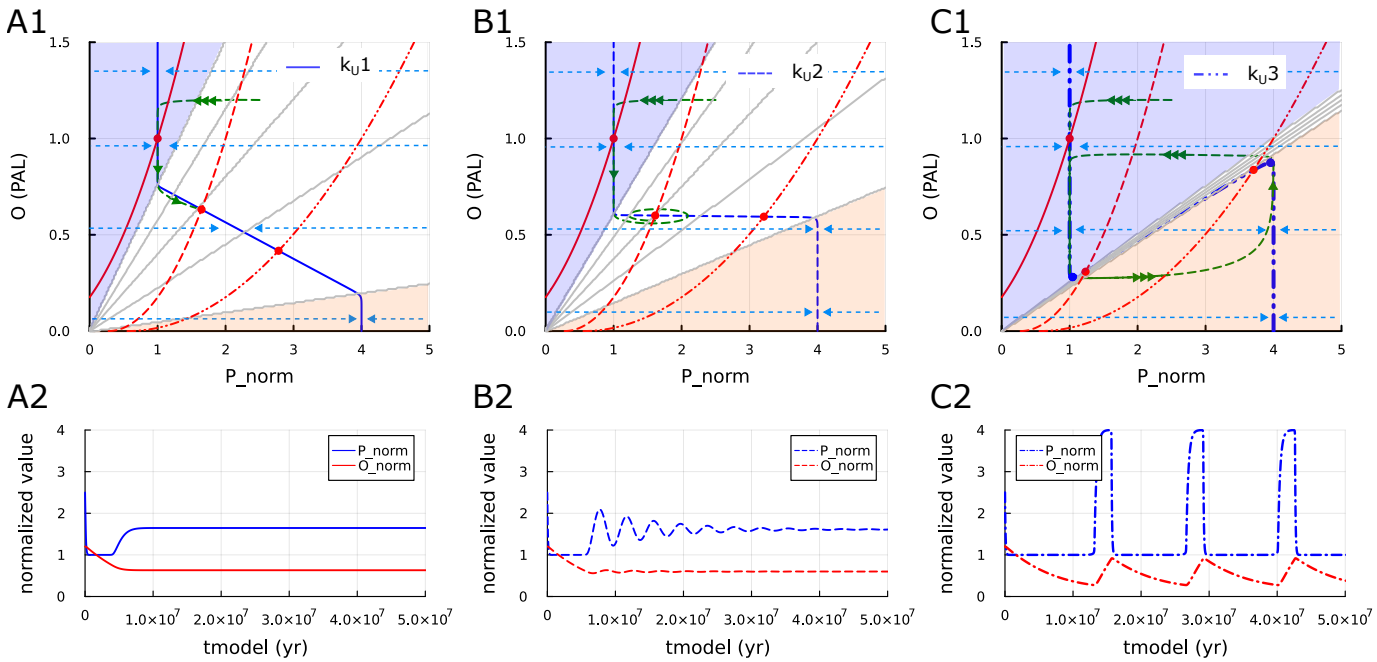

Fig. 4. Timescale separation and the phase plane geometry of phosphorus and oxygen nullclines determine the dynamics and local and global stability of the coupled marine phosphorus - atmosphere/ocean oxygen system. Columns show phosphorus-oxygen phase plane (upper panels) and a representative time series (lower panels) for the three different marine burial flux distributions considered in Fig. 3. Phase plane (**A1**) shows the globally stable case (k_U1) where the critical manifold (solid blue) is everywhere attracting; (**B1**) the neutral stable case (k_U2) where the critical manifold (dashed blue) is parallel to fast fibres (dashed light blue); (**C1**) the unstable case (k_U3) where the critical manifold has a repelling region separated from the two attracting regions by folds (blue dots). Contours of organic-carbon-burial-weighted ocean floor anoxia = (0.0, 0.25, 0.5, 0.75, 1.0) are shown in light grey, fully oxic and anoxic regions are shown with light blue and orange shading respectively. Three dO/dt=0 nullclines (dash-dot, dashed, solid red lines) are shown for increasing values of overall global organic carbon to phosphorus burial ratio. The dashed green line in the upper panels and time series in lower panels shows an example of adjustment starting from an arbitrary point (with P=2.5, O=1.2) for the middle (dashed) oxygen nullcline: as a result of timescale separation the system rapidly reaches the critical manifold and then adjusts slowly towards the oxygen nullcline. If the oxygen nullcline intersects an attracting region then the system reaches a stable equilibrium (**A1**, **A2**). If it intersects the repelling region (**C1**, **C2**) a limit cycle oscillation results, composed of slow segments closely following the critical manifold, with fast jumps at fold points.

at (low) oxic or (high) anoxic values. At intermediate values (where ocean floor redox is changing), the shape of the critical manifold reflects the productivity and anoxia controls on global marine phosphorus burial discussed in the previous section. When phosphorus burial increases monotonically with phosphorus (case k_U1, corresponding to burial in a broad range of redox environments), the critical manifold is "attracting" everywhere (where fast fibres approach the critical manifold) (Fig. 4 A). When marine phosphorus burial flux is a non-monotonic function of phosphorus (case k_U3, corresponding to all burial in a uniform redox environment), two corresponding "fold points" will appear in critical manifold, with a "repelling" segment between the fold points (where fast fibres leave the critical manifold) (Fig. 4 C). An intermediate value of redox heterogeneity can produce a neutrally stable case (case k_U2), where a part of the critical manifold runs parallel to the fast fibres (Fig. 4 B). This corresponds to a "hysteresis bifurcation" (*58*), with two folds and a repelling region appearing as the redox heterogeneity is reduced.

As shown in Fig. 4 A1, if the critical manifold is attracting everywhere, initial evolution along a fast fibre is always followed by slow evolution along a slow manifold (close to the singular manifold) until the oxygen nullcline is reached, and the system is globally stable. If the system has fold points as in Fig. 4 C1, then stability depends on the oxygen nullcline: if it intersects an attracting region, the result is a stable equilibrium; whereas if it intersects a repelling region, the result is a limit cycle oscillation, composed of fast and slow segments with jump points near folds. As the fast fibres are at constant oxygen, this analysis shows that (in the singular limit of complete timescale separation) the criteria for neutral stability of the coupled system (that part of the critical manifold runs parallel to the fast fibres, Fig. 4 B1) is in fact identical to the criteria for monotonic vs non-monotonic phosphorus burial discussed in the previous section. To define this global stability property in a general way, we introduce a "fold sharpness" metric based on the relative position of the folds on the critical manifold

(see formula in Supplementary Materials Eq. S14), where values of < 0 corresponds to global stability, 0 to neutral stability, range 0 - 1 to unstable systems with a folded critical manifold, and 1 to the maximal "sharp switch" case. With finite timescale separation, linear stability analysis (Materials and Methods) shows that stability is slightly increased, with the system remaining globally stable providing that the angle between the critical manifold and fast fibres is less than the ratio of timescales $\approx \tau_P/\tau_O$.

The oxygen nullcline is controlled by the balance between the marine organic carbon burial source, and sinks from oxidative weathering and reduced tectonic and metamorphic inputs. In our minimal model (*i.e.* prior to the evolution of a terrestrial biota and hence a fire feedback control), marine organic carbon burial is proportional to P and oxidative weathering is proportional to $O^{1/2}$, hence the oxygen nullcline is approximately a line with $O \propto P^2$. We represent the effect of secular evolution of $p\mathrm{O}_2$ over Earth history by an increase in overall marine organic carbon burial flux (*i.e.* parameterized using an overall modifier on the Corg:P ratio, parameter Corg burial factor), and show three illustrative cases in Fig. 4 *A*-*C* (red lines): (i) marine organic carbon burial of half the modern value, resulting in lower Proterozoic oxygen level; (ii) a modern value for marine organic carbon burial ($4.5\times10^{12}\,\mathrm{mol\,yr^{-1}}$ at modern $P = P_0$ (*33*)) resulting in a Neoproterozoic / Paleozoic oxygen level, still with an anoxic ocean; (iii) as a test of model consistency only, including in addition a prescribed constant modern land organic carbon burial of $4.5 \times 10^{12}\,\mathrm{mol\,yr^{-1}}$ resulting in a modern Earth steady state (with $O/O_0 = 1$ and $P/P_0 = 1$) and an oxic ocean. If the critical manifold is folded, this leads secular evolution through singular Hopf bifurcations as the oxygen nullcline crosses folds (*58*), from a stable Proterozoic regime with anoxic ocean, through a limit cycle oscillation regime, to a stable Phanerozoic regime with oxic ocean.

This analysis connects system-level behaviour to biogeochemical processes and secular evolution and geometrically identifies the nature of the system-level feedback controls on stability

and on the limit cycle oscillations in phosphorus-oxygen only models identified by (*31, 39*).

Carbon cycle and phosphorus weathering feedbacks do not qualitatively change the criteria for stable and oscillatory regimes

We now include the carbon cycle (Eq. 3) and examine how the phosphorus weathering feedbacks due to oxygen, and to temperature and hence $p\mathrm{CO}_2$ level modify the regimes identified in the phosphorus-oxygen only system. There are now three state variables, requiring a generalization of the dynamical systems framework and phase space to three dimensions (Fig. 5), now including a third dimension for A (total atmosphere-ocean carbon). The critical manifold ($dP/dt = 0$ nullcline) and $dO/dt = 0$ and $dA/dt = 0$ nullclines are now surfaces, and the steady-state equilibrium point corresponds to the intersection of all three surfaces. There is now a dependence of the critical manifold on A (and hence $p\mathrm{CO}_2$) due to increased phosphorus weathering input as temperature and $p\mathrm{CO}_2$ increase. There is also a potential additional dependence on oxygen due to the oxygen sensitivity of phosphorus weathering (not present in this baseline scenario, but shown in Supplementary Materials Fig. S9).

The phase plane diagram demonstrates how the stability criteria generalize from the two-dimensional phosphorus-oxygen system. In the singular limit (with infinite timescale separation), if there is no fold in the critical manifold the system is globally stable (Fig. 5 *A*). If the critical manifold surface is folded, there are attracting and repelling regions now separated by fold lines, and stability depends on the location of the equilibrium point now controlled by the intersection of oxygen and carbon nullclines on the critical manifold surface (Fig. 5 *B, C*). Finite timescale separation slightly increases stability resulting in a small correction to the stability boundary (see linear stability analysis in *Materials and Methods*, blue dashed line in regime summary Fig. 10).

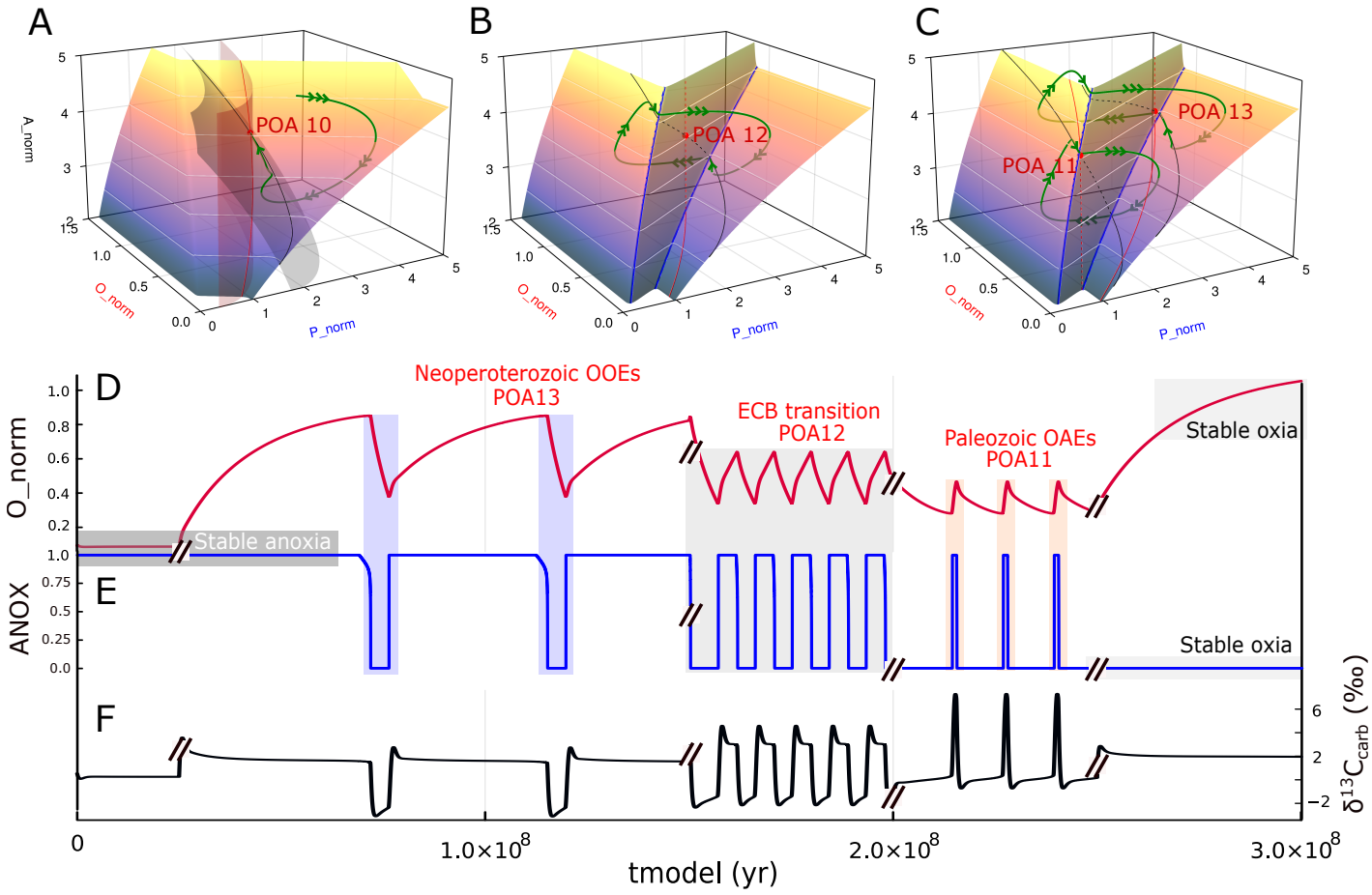

Fig. 5. Dynamics and stability of the coupled phosphorus, oxygen and carbon system, including feedbacks due to phosphorus weathering. (**A**) phase plane for a "globally stable" case, showing the dP/dt=0 nullcline surface (the *critical manifold*), and the dO/dt=0 (red) and dA/dt=0 (black) nullcline surfaces and intersections with the critical manifold. During the adjustment to a steady-state (green line), the three-timescale system rapidly reaches the critical manifold (dP/dt = 0 nullcline) (fast line segment with triple arrows), then evolves at almost constant oxygen until it reaches the A nullcline (medium-slow line segment with double arrows), and then evolves to oxygen source-sink balance at the dO/dt = 0 nullcline (slow line segment with single arrow). (**B**) as panel (**A**), showing limit cycle oscillations for an unstable case. The critical manifold is now folded with repelling and attracting regions, and the limit cycle contains segments with medium-slow and slow evolution along the dA/dt=0 and dO/dt=0 nullclines in the critical manifold, and fast jumps when a fold is reached. (**C**) as panel (**B**), showing limit cycles in marginally unstable near-anoxic (POA 13) and near-oxic (POA 11) cases. (**D-F**) Time series of atmospheric oxygen level, ocean anoxia, and carbon isotope for a sequence of regime changes from POA 13 to POA 11.

Nullcline geometry determines event duration and oscillation period

The dynamical systems analysis demonstrates that there are two major controls on the periodicity and "waveform" (relative timing of oxic and anoxic intervals) of the limit cycle oscillation regime, as well as a third control on both event duration and oscillation period that is unique to the oxygen-carbon-phosphorus system.

The first control is via the location of crossing point of the oxygen nullcline and the repelling part of the critical manifold. If the unstable equilibrium point is near the stable anoxic regime, then the system spends most of its time drawing down carbon and then slowly accumulating oxygen, with a fast excursion around the rest of the oxic part of the limit cycle. Similarly, if the system is close to the stable oxic regime, the ocean is oxic for the majority of the time with fast excursions around the anoxic part of the limit cycle. The oscillation period therefore increases as the unstable equilibrium point approaches the fold and marginally stable regime, whereas the duration of the fast excursion events are approximately constant (compare *e.g.* cases POA 12 and POA 13 in Fig. 5 panels *D, E, F*; qualitatively similar results for the phosphorus-oxygen only system are shown in Supplementary Materials Fig. S6).

The second control on oscillation period is via the "sharpness" of the fold in the critical manifold. The behaviour of the oxygen-phosphorus system (Fig. 4) illustrates the mechanism: the majority of the time during the limit cycle oscillation is spent during the slow increase and decrease of oxygen, hence the "sharp switch" case shown in Fig. 4 *C*, with the largest oxygen excursions, has the longest oscillation period. As the range in oxygen between the two folds becomes smaller, the oxygen excursions around the limit cycle oscillation become smaller and the oscillation timescale is reduced. As the phosphorus nullcline approaches the neutrally stable case (Fig. 4 *B*), timescale separation breaks down and the oscillation period scales as the geometric mean of the phosphorus and oxygen timescales, *i.e.* $(\tau_P\,\tau_O)^{0.5}$, where this provides a lower limit on the period of coupled oscillations in the P-O system (derivation in Materials

and Methods). For the parameters shown, the oscillation period is reduced from $\approx 12\,\mathrm{My}$ for the sharp switch case to $\approx 4.7\,\mathrm{My}$ for the neutrally stable case (see additional numerical experiments in Supplementary Materials Fig. S5).

The third control is unique to the oxygen-carbon-phosphorus system, where the limit cycle (Fig. 5 *B*, *C*) may or may not include a slow segment controlled by oxygen, leading to a possible phosphorus-carbon regime with faster event duration and oscillation timescale. Once a trajectory reaches a stable part of the critical manifold, there is a medium-slow adjustment of carbon at nearly constant oxygen. However, there is now the possibility of two qualitatively and geometrically different types of behaviour: if the medium-slow part of the trajectory reaches a fold before it reaches the dA/dt=0 nullcline, there is no slow adjustment of oxygen, conversely if the medium-slow part of the trajectory reaches the dA/dt=0 nullcline before it reaches the fold there is a slow adjustment of oxygen until the fold is reached. The characteristic duration of the oxic or anoxic event now depends on whether oxygen is involved: if the trajectory reaches the dA/dt=0 nullcline, requiring a slow adjustment of oxygen, then the characteristic duration is $\approx 4\,\mathrm{My}$ (as for the anoxic background/OOE case POA 13 in Fig. 5); if the trajectory during the event reaches the fold before the dA/dt=0 nullcline, then the characteristic duration is $< 1\,\mathrm{My}$, controlled by the carbon timescale (as for the the oxic background/OAE case POA 11 in Fig. 5).

As for the P-O model, decreasing the "sharpness" of the fold in the range $0.4 - 1.0$ reduces the oscillation period in the oxygen-controlled regime (summarized in Fig. 10), with an additional further reduction due to a transition to a phosphorus-carbon controlled regime for sharpness ≤ 0.4. In this regime, the limit cycle does not reach the dA/dt=0 nullcline at either extreme, and faster limit cycle oscillations (period $\approx 2 - 3\,\mathrm{My}$) with no dynamical involvement of oxygen are now possible (case POA 1033 in Supplementary Materials Fig. S12). These are primarily driven by weathering feedbacks and the carbon cycle: high organic carbon burial in

the anoxic state draws down CO_2 and reduces phosphorus weathering, reducing ocean nutrient level and driving a transition back to an oxic ocean. As the carbon reservoir is smaller than the oxygen reservoir, the limit cycle is now primarily in the P - A plane, with only small changes in oxygen. Sensitivity studies (Materials and Methods, Supplementary Materials Fig. S10, S11) show that either higher degassing and hence silicate weathering, or a smaller organic carbon cycle size would increase the influence of oxygen and reduce the size of this regime.

Secular trends in stability and periodic variability of ocean oxygen are generic properties of system dynamics

This analysis shows that secular evolution from a regime with stable ocean anoxia, through an unstable oscillatory regime, to a stable oxic regime is a generic property of the system dynamics. It also shows that, superimposed on the overall secular trend towards increasing atmospheric oxygen, a decrease in atmospheric oxygen from the end of the Neoproterozoic anoxic to the beginning of the Phanerozoic oxic regime consistent with the Ce isotope records (*4*)) (see Fig. 4 C1, Fig. 5 D) is a consequence of the same nullcline geometry that leads to an unstable intermediate regime.

These results also show that secular evolution in the pattern of variability in ocean oxygen in the unstable oscillatory regime (Fig. 5, Fig. 10), from widely-spaced Neoproterozoic OOE in an anoxic background (e.g. the Shuram excursion (*11*)), through increasingly frequent OOE (*7*), to an early Cambrian oscillatory regime (*13*), to increasingly widely-spaced Paleozoic OAE in a predominantly oxic background (*12*) is an additional consequence of dynamical constraints. However, the longest-duration limit cycles (with widely spaced events) are a result of the very slow evolution in a marginally-unstable regime near the fold, and hence are unlikely to be realised in the presence of inevitable changes in tectonic and other forcings. A consistent model therefore needs to consider the interaction of such "noise" or stochastic forcing with the

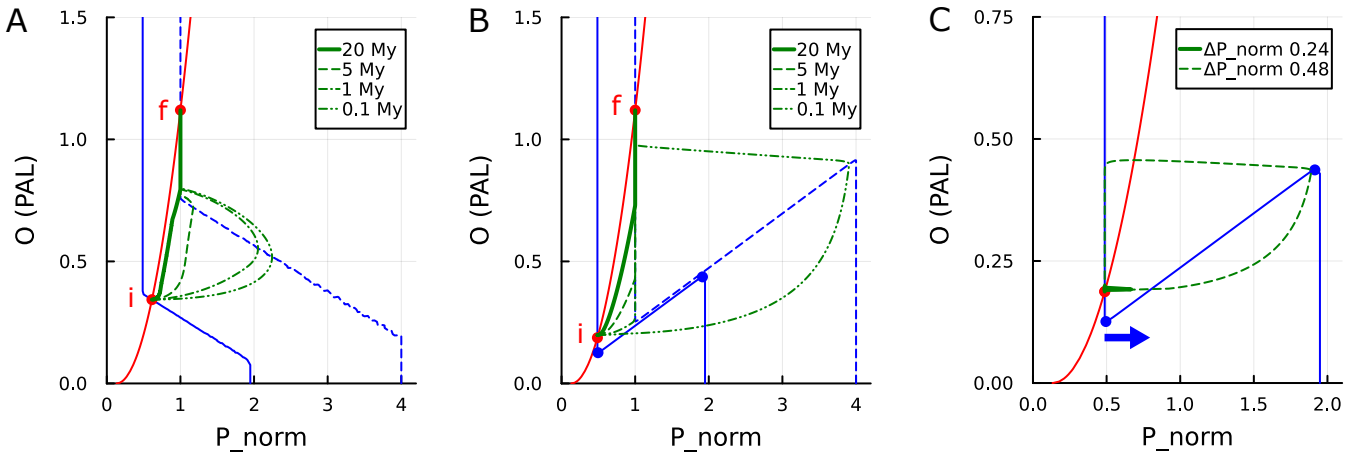

Fig. 6. Rate-dependent forcing and excitation of an OAE in the phosphorus-oxygen model. (**A**) Rate-dependent response of a globally-stable system to a linear increase in phosphorus weathering input, driving evolution from an initial steady-state i to final steady-state f. If the rate of increase is slow relative to the oxygen timescale, the system approximately tracks the oxygen nullcline during the adjustment process and the ocean remains oxic. A faster rate results in a large increase in P amplified by the development of anoxia before oxygen can rise. (**B**) as panel (**A**), for a system in the excitable regime with a marginally stable oxic initial state close to a fold. A fast increase in P input results in a limit cycle excursion, as the oxygen response time is too slow to allow the trajectory to intercept the fold. (**C**) excitation of an OAE by a short-duration pulse in phosphorus input. The steady-state is oxic and near to a fold. A small phosphorus pulse leads to a small response; a pulse larger than a threshold value (sufficient to cross the repelling branch of the critical manifold, size indicated by blue arrow) generates a limit cycle excursion. See Supplementary Materials Fig. S7 for full details.

nonlinear dynamics.

Rate-dependent changes in forcing may destabilise the system and drive OOE or OAE

Parameter changes at finite rates ("parameter ramping" in the terminology of (*51*)) can also drive "rate dependent" tipping (*46, 51, 52*) where the system fails to track a continuously changing quasi-static attractor.

We show an example with the phosphorus-oxygen system in Fig. 6 *A*, where an increase in phosphorus weathering on a timescale that is short compared to the oxygen timescale can drive

an OAE event even in a system that is globally stable, due to the short phosphorus timescale and non-linear amplification by the redox dependence of phosphorus burial. An excitable system (with a folded critical manifold) can show a more dramatic rate-dependence, with threshold behaviour where the ramping rate is sufficient to allow a trajectory to pass a fold, generating an excursion around a limit cycle (Fig. 6 *B*).

The P-O-A system may also show excitations in response to rate-dependent changes in $\mathrm{CO_2}$ input (from metamorphic, mantle or Large Igneous Province (LIP) emplacement, (*66*)), where the rate of change is fast relative to the oxygen timescale. The cases most relevant to interpreting the Neoproterozoic-Paleozoic record are where a decrease in degassing in an anoxic system excites an OOE event, and where an increase in degassing in an oxic system excites an OAE event: these could correspond to the trailing and leading edge respectively of an interval of enhanced $\mathrm{CO_2}$ input due to LIP emplacement. We discuss here the OOE case (Fig. 7) and show the OAE case in Supplementary Materials Fig. S14. A decrease in $\mathrm{CO_2}$ input results in a new anoxic steady-state with a decrease in P weathering input, steady-state oxygen, and A and hence $\mathrm{CO_2}$ (as P input $\propto$ degassing if as here P input is largely due to silicate weathering, $O \propto$ the square of organic carbon burial and hence of P input, and $\mathrm{CO_2}$ decreases as a result of the silicate weathering feedback). However, if the rate of decrease is fast relative to the oxygen timescale, the system evolution along the critical manifold cannot track the oxygen nullcline, and may reach a fold and result in an OOE excursion around a limit cycle.

This regime is most relevant to a low-oxygen, pre-land-plant world, as the large degassing-driven changes in steady-state atmospheric oxygen are a result of the lack of land-plant fire feedback control (*32*). The OOE excitation case suggests a possible causal link between a reduction in degassing that ultimately leads to a glaciation, and a preceding negative carbon isotope excursion.

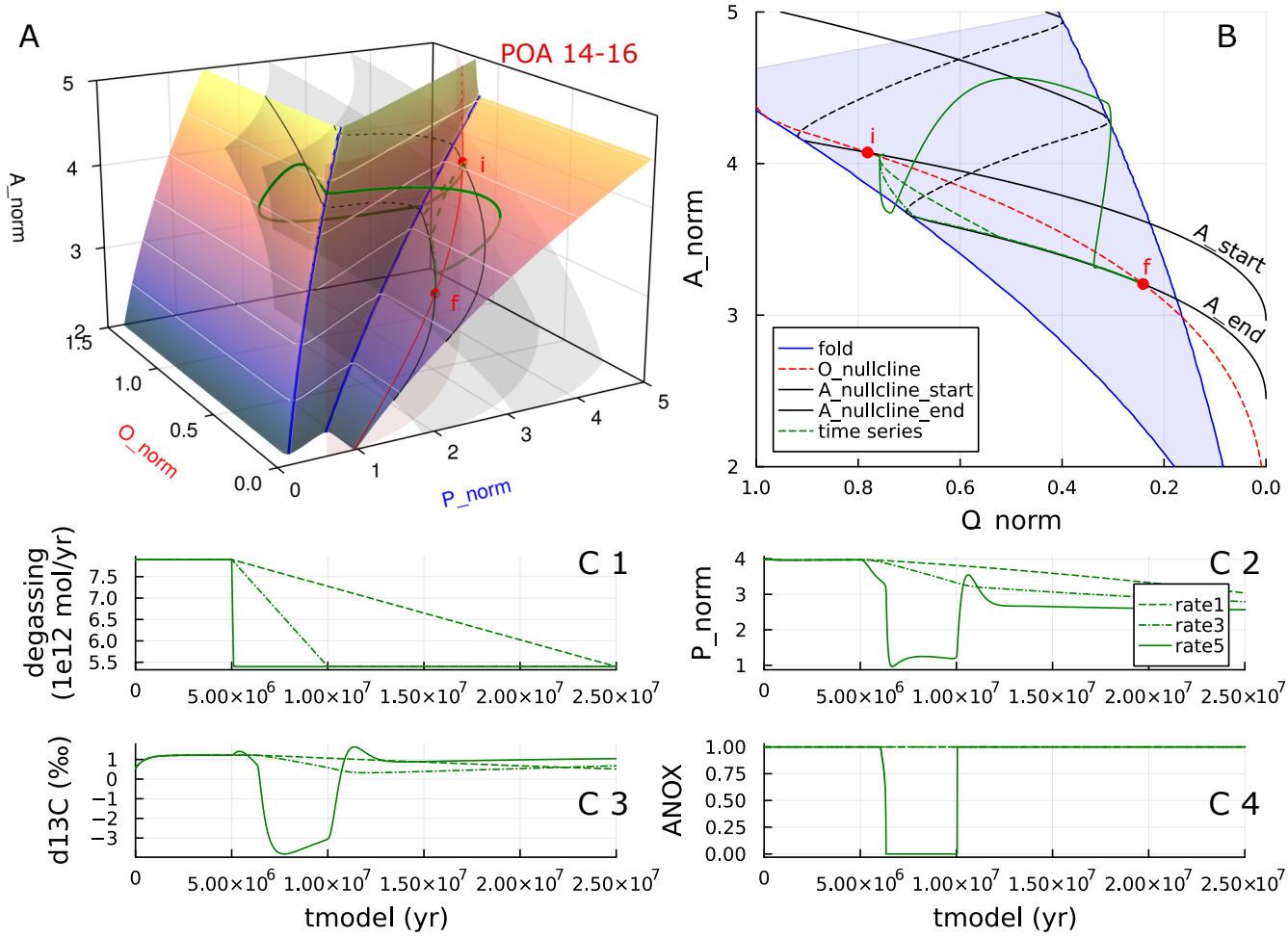

Fig. 7. Excitation of an OOE event by a rate-dependent reduction in degassing. The system is initially in a marginally stable steady-state with anoxic ocean at point i. A slow linear reduction in degassing forcing of $2.5 \times 10^{12}\mathrm{mol/yr}$ (32 % of total degassing flux) relative to the oxygen timescale (dashed green line, reduction over 20 My) results in the system remaining anoxic, with the adjustment process to final steady state f approximately following the dO/dt=0 nullcline and remaining in the attracting anoxic sheet of the critical manifold. A fast reduction in degassing (solid green line, reduction over 0.1 My) results in the initial adjustment trajectory at approximately constant oxygen reaching the fold, tipping the system to a limit cycle and OOE (duration $\approx 4\mathrm{My}$). The rate threshold for excitation of an OOE (where the trajectory reaches but doesn't cross the fold) is approximately 5 My (dash-dot green lines). Panel (**A**) shows the P-A-O phase space, panel (**B**) shows a projection of the phase space onto the O, A plane with the overlap of the folded critical manifold indicated by blue shading, panels (**C 1-4**) show the time series of CO_2 degassing forcing, phosphorus, $\delta^{13}C$, and marine-burial-weighted anoxia.

OOEs and OAEs may be excited by small perturbations

A system is *excitable* if it has a stable equilibrium where applying a small perturbation leads to a small excursion, whereas a larger perturbation is amplified by the systems internal dynamics and leads to a large response before eventual return to the equilibrium (*40, 45, 48*). Multiple-timescale dynamical systems exhibit this behaviour in a regime where the steady-state is located on a stable attracting region of the critical manifold close to a fold, where a perturbation (either to a state variable or to a parameter that moves the location of the critical manifold) that exceeds a threshold moves the system outside of the domain of stability resulting in a trip around the limit cycle, with a characteristic size and timescale that is a property of the system parameters, not of the applied perturbation.

The mechanisms and thresholds for excitability are clearest in a two-dimensional system. We show an example of excitation of an OAE in the phosphorus-oxygen model by a transient increase in phosphorus weathering (*e.g.* by early land plants (*34, 67*), see also (*68*)) in Fig. 6 *C*. This represents a perturbation to the fast phosphorus state variable, where the excitation threshold is determined by the distance from the stable equilibrium point to the repelling part of the critical manifold. A small phosphorus pulse leads to a small response; a pulse larger than a threshold value (sufficient to cross the repelling branch of the critical manifold, size indicated by horizontal blue arrow) generates a limit cycle excursion. The criteria for an excitation by a hypothetical negative perturbation to the slow oxygen variable (not shown) would be set by the distance from the stable equilibrium point to the fold.

Including the carbon cycle in the now three-dimensional system makes it possible to represent interactions with tectonic $\mathrm{CO_2}$ input. We show an example of excitation of an OAE event by a short-timescale $\mathrm{CO_2}$ input pulse (*e.g.* from LIP emplacement, (*66*)) in Fig. 8. The $\mathrm{CO_2}$ input (on a timescale $\leq 10^4\mathrm{yr}$) drives an effectively instantaneous change in the A state variable (*i.e.* on a timescale short relative to the other timescales in the system). The initial

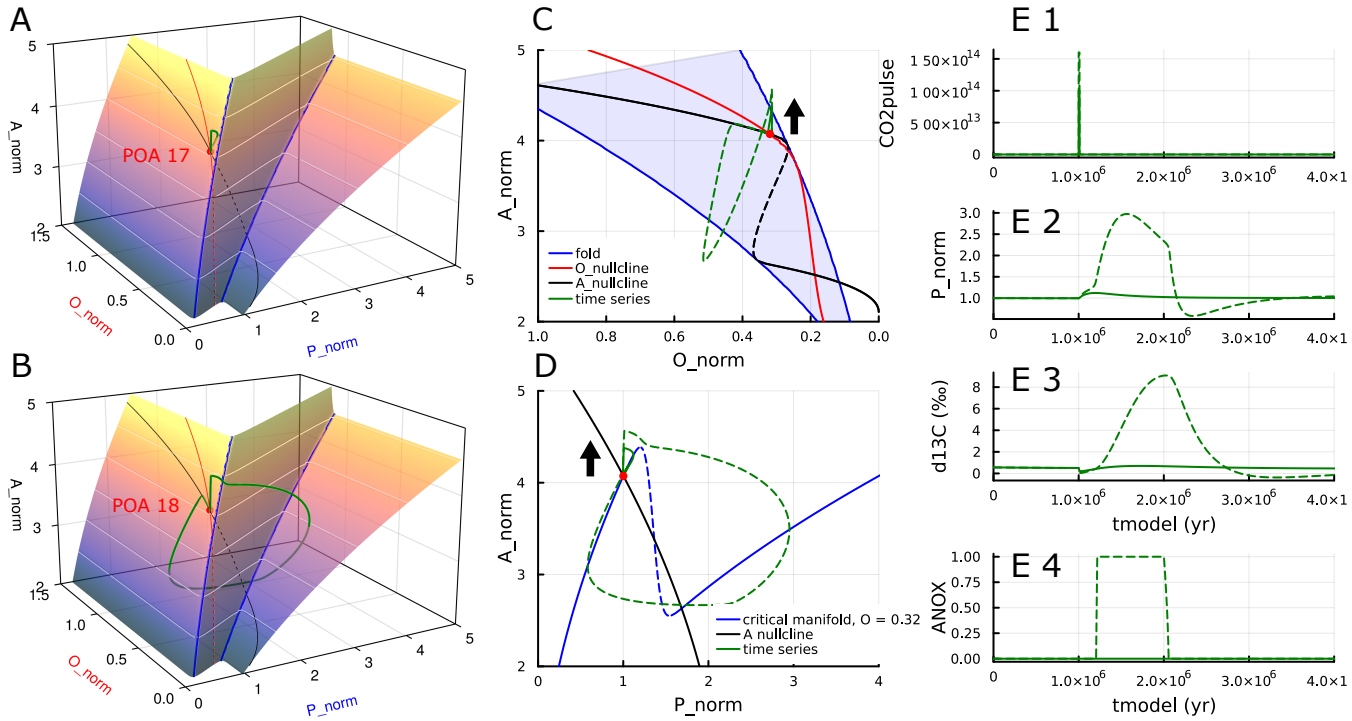

Fig. 8. Excitation of an OAE by a short-duration tectonic CO_2 input. The system is initially in a marginally stable steady-state with oxic ocean, and is perturbed by a CO_2 pulse of duration = 10^4yr *i.e.* short relative to the A adjustment timescale. (**A**) a CO_2 input of 1×10^{18}mol results in a small response and adjustment back to the initial steady state. (**B**) a CO_2 input of 1.6×10^{18}mol (larger than the threshold required for a trajectory to cross the nearby fold) results in a large limit cycle response as increased P weathering drives the ocean anoxic, with an anoxic interval duration of 800 kyr and $> 5 \times 10^6$yr required to return back to the initial steady state. Note that there is no slow oxygen-controlled segment controlling the duration of the anoxic interval. Panel (**C**) shows a projection of the phase space onto the O, A plane with the overlap of the folded critical manifold indicated by blue shading, panel (**D**) shows a cut through phase space at constant oxygen. Excitation threshold is indicated by a vertical black arrow. Panels (**E 1-4**) show time series of CO_2 forcing, phosphorus, $\delta^{13}C$, and marine-burial-weighted anoxia.

system response is then for phosphorus to evolve along a fast fibre. If this trajectory intersects an attracting region of the critical manifold, then the response to the perturbation is small (Fig. 8 *A*). If this trajectory goes past a fold then it results in a large excursion around a limit cycle (Fig. 8 *B*).

The phase plane approach introduced here therefore shows how the combined effect of

global stability (*cf.* (*31*)), intrinsic instability (*cf.* (*39*)) and tectonic forcing may interact to drive OAE events, and also reveals the controls on excitation threshold, event response, and event duration. The primary control on the excitation threshold is the location of the equilibrium point relative to the fold (Fig. 8 *C*, *D*). Cooling during an OAE event occurs if A and hence CO_2 at the initial steady-state is at a higher value than the lowest value reached during the limit cycle excursion: this provides a causal mechanism to link glaciation to Paleozoic OAE as seen in the Hirnantian (*17*) and hypothesized OAE accompanying Silurian carbon isotope excursions (*69*). The limit cycle excursion shown in Fig. 8 also does not include a slow oxygen segment during the anoxic part of the excursion and hence produces a relatively short anoxic event (in contrast to the hypothesis of (*39, 65*)), where the sensitivity studies (Materials and Methods, Supplementary Materials Fig. S10-S11) illustrate the parameters that control whether oxygen is involved and hence this control on OAE event duration.

Secular evolution combined with excitation by stochastic forcing explains Neoproterozoic to Paleozoic variability

The phase plane geometry shows that the stability relative to small perturbations is controlled by the position of the equilibrium point relative to either a fold (Fig. 8) or a repelling segment (Fig. 6) of the critical manifold. As the oxygen nullcline moves past folds during secular evolution over Earth history, the transition from stable to oscillatory regimes must also pass through marginally stable and unstable regimes that are susceptible to small perturbations in forcings or parameters. The dynamical systems analysis can be used to investigate specific mechanisms, ie how sea-level change, Milankovitch cycles, and variability in degassing fluxes modify stability and excite events, either by perturbing state variables or by moving the location of nullclines. However, as the perturbations required are small and the event signature is dominated by the system internal dynamics, the overall patterns in event probability (or intervals between events)

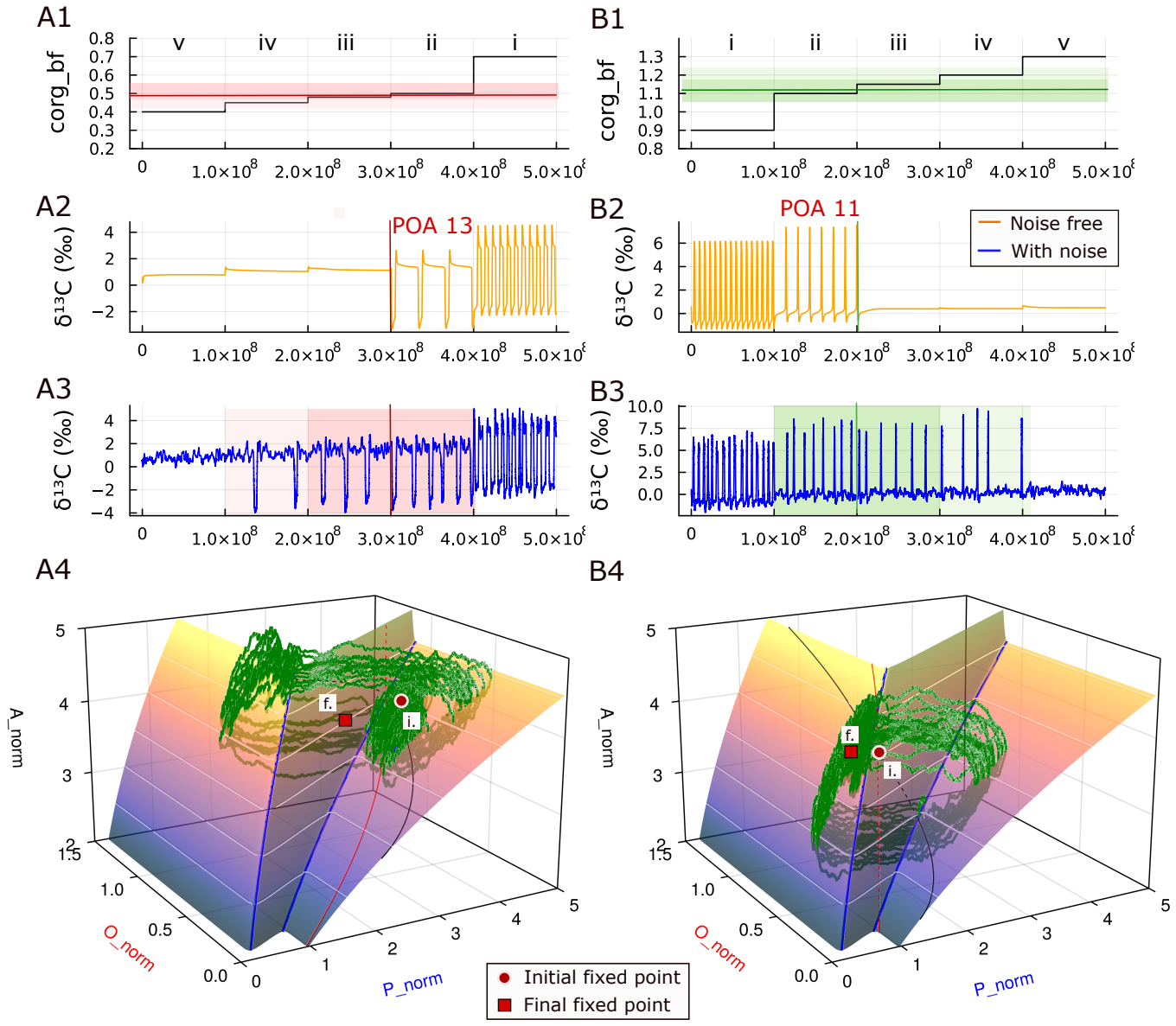

Fig. 9. Dynamics and stability of the coupled phosphorus, oxygen and carbon system, including stochastic forcing applied to CO_2 input. Left column shows stepwise evolution from stable anoxic to limit cycle regime, right column shows stepwise evolution from limit cycle to stable oxic regime. (**A1**) and (**B1**) show the carbon burial parameter used to move the oxygen nullcline through stable and unstable regimes. Green and red lines and shadings indicate fold locations and marginally unstable and stable (excitable) regimes (cf Fig. 10). (**A2**) and (**B2**) show the time series for the noise-free system, showing stable and limit-cycle regimes as in Fig. 5. (**A3**) and (**B3**) show the effect of stochastic forcing: in the marginally unstable regime (ii) the limit cycle becomes quasi-periodic and shorter on average; the marginally stable regime (iii) now shows similar quasi-periodic limit cycles, and the marginally stable regime (iv) shows random widely-spaced events. (**A4**) and (**B4**) show time series in the phase plane.

and interactions with system dynamics are a property of the statistics of generic small perturbations and the dynamical regime, and are largely independent of the mechanism.

As an example of a generic "small perturbation" we consider a small random stochastic variability in tectonic and metamorphic CO_2 input, represented by a "standard white noise", Eqn. 10 (*49, 50*). The white noise amplitude is chosen to generate normally distributed fluctuations in degassing CO_2 input with expectation $\approx 10^{12}\,\mathrm{mol\,yr^{-1}}$ when averaged over $10^6\,\mathrm{yr}$ intervals, or $\approx 13\,\%$ of the mean degassing input. We show the effect this has on the transition between stable and unstable regimes in Fig. 9, for both the Neoproterozoic stable anoxic to oscillatory transition and the Paleozoic oscillatory to stable oxic transition. The stochastic forcing has little effect on the intrinsically unstable regime (i) when the equilibrium point is far from the fold, or on the stable regime (v) (where the noise produces a $\approx 0.5‰$ fluctuation in the model carbon isotope time series, consistent with that seen in the geological record (*18*)). When the system is in the marginally unstable regime (ii), the stochastic forcing speeds up the oscillation period as limit cycles are truncated before reaching the folds, and effectively sets an upper limit on the limit cycle oscillation period which can no longer increase arbitrarily as the equilibrium point approaches the fold. In the marginally stable regime (iii) where the threshold distance is comparable to the noise amplitude, quasi-periodic limit cycles are generated; this quasiperiodic limit cycle behaviour is similar in both the marginal unstable and stable regimes (ii) and (iii). In the marginally stable regime (iv) where the threshold distance is large relative to the noise amplitude, intermittent widely-spaced events are produced where the mean interval between events depends on the noise amplitude and threshold distance (*49*). We therefore predict a marginally stable late Neoproterozoic regime (Fig. 9 *A3* regimes iv, iii, ii) with an increasing probability of stochastically excited OOE events (*13*), and a marginally stable early Paleozoic oxic regime (Fig. 9 *B3* regimes ii, iii, iv) with a decreasing probability of stochastically excited OAE events (*14, 16, 17*) through the Phanerozoic.

We summarize the model stability regimes in Fig. 10, as a two-dimensional space spanned by a parameter controlling the folding of the critical manifold (determined by the distribution of marine burial fluxes in the model), and a parameter controlling the position of the oxygen nullcline (determined by oxygen source-sink balance, and represented by an organic carbon burial factor in the model). As organic carbon burial flux increases over the past billion years of Earth's history (*70*) the Earth system moves through oxygen regulation regimes, starting from a Proterozoic stable anoxic regime with atmospheric oxygen weakly regulated by oxidative weathering (*32*) and an anoxic ocean. There is then an increasing probability of exciting OOE events (*13*), followed by a singular Hopf bifurcation as the oxygen nullcline crosses a fold into a limit cycle oscillation regime (*31*), where we predict a secular evolution from long-period primarily anoxic intervals with OOE, to shorter equally spaced oxic-anoxic oscillations (*13*), to long-period primarily oxic intervals with OAE. This is followed by an early Paleozoic oxic regime as the oxygen nullcline crosses the second fold, with a decreasing probability of exciting OAE events as atmospheric oxygen increases.

Discussion

Our results reveal that the major controls on the dynamics and global stability of the coupled biogeochemical cycles of marine phosphorus, atmosphere-ocean carbon and oxygen can be understood from the phase space geometry of the multi-timescale system. The overall long-timescale dynamics are controlled by the phase-space structure of the slow variables in the system, hence as for biological systems (*47, 48*), this structure can be used to identify and classify dynamical regimes. The major patterns in the Neoproterozoic to Paleozoic geochemical record follow from the hypotheses that phosphorus is the limiting nutrient controlling the net oxygen source from organic carbon burial, and that the redox-sensitivity of marine phosphorus burial (*37,38*) introduces a potential instability identified by a folds and a repelling region in the

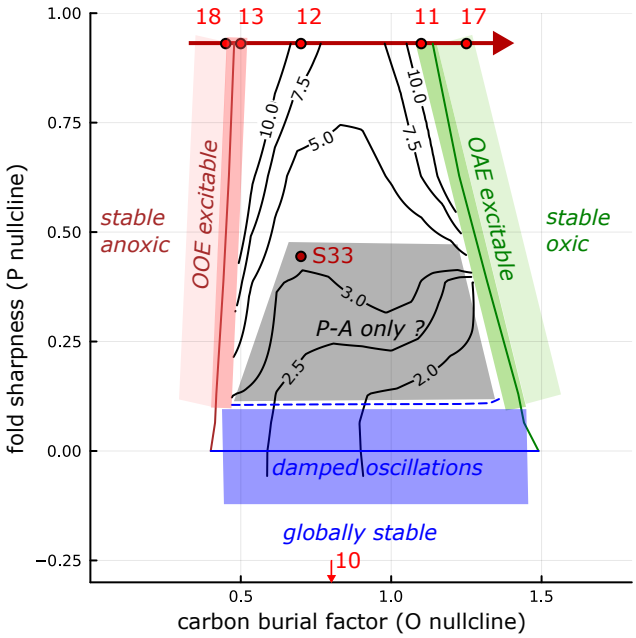

Fig. 10. Stability regimes for coupled phosphorus-oxygen-carbon model. Secular evolution over Earth history corresponds to evolution from the Proterozoic at left to Phanerozoic at right. Vertical axis: "sharpness" of fold in critical manifold, where the globally stable regime is approximately bounded by a solid blue horizontal line at a "hysteresis bifurcation" (*58*) (valid in the singular limit of complete timescale separation), and actually bounded by the dashed blue line (determined by linear stability analysis for the finite-timescale separation numerical model). Horizontal axis: organic carbon burial parameter, where brown and green vertical lines indicate singular Hopf bifurcations as the oxygen nullcline crosses folds, and shaded areas show marginally stable excitable regimes. Contours show limit cycle oscillation period in My. Grey shaded region shows possible phosphorus-carbon only faster limit cycle oscillation regime. Blue shaded region shows regime where the approach to stable equilibrium is via a damped oscillation. Red dots with numbers correspond to the POA model experiments shown in the main paper (Figures 5, 8, and 7) and Supplementary Materials, see Table S4 for full list of model parameters used. Red arrow: secular increase of overall organic carbon burial flux details in Fig. 5. Dark red and green shadings: the marginally unstable and stable regimes dominated by stochastic forcing. Light red and green shadings: marginally stable regimes with random events excited by stochastic forcing, details in Fig. 9.

critical manifold (the nullcline of the fast marine phosphorus variable). This introduces both an unstable limit-cycle-oscillation regime, and marginally (un)stable excitable regimes. The dynamical systems approach can thereby help disentangle system-level vs process-level and internal-dynamics vs externally-forced explanations of the geochemical record.

Dynamical systems analysis disentangles system-level and process-level explanations

Our analysis implies that major patterns in the variability and secular evolution of the Neoproterozoic to Phanerozoic biogeochemical record are generic properties of the phosphorus-carbon-oxygen dynamical system, independent of detailed assumptions about the biogeochemical processes involved. A hierarchy of models is therefore required to apply consistency constraints between the process and system level, and enable testing of hypotheses against both local datasets and global timeseries. One strategy is to exploit timescale separation to combine long-timescale low-dimensional biogeochemical models with explicit calculation of spatial and temporal averaging using offline "snapshots" of spatially-resolved climate or ocean models (cf (*54*)). Examples of this approach applied to land surface weathering include the GEOCLIM series of models (*71*), SCION (*72*), and the representation of oxidative weathering in (*32*); the intermediate-complexity ocean model used here provides an example of this approach applied to marine burial fluxes. A complementary approach is to use the theoretical insights derived from low-dimensional models to interpret and synthesise the results from fully-coupled spatially-resolved Earth system models, which are necessarily limited by computational constraints to short timescales and limited regions of parameter space.

Excitability is a consequence of non-linear feedbacks that are sufficient to cause oscillation

The geometrical phase plane analysis demonstrates that if non-linear feedbacks in marine phosphorus burial can create an unstable oscillatory regime, there must also be adjacent marginally (un)stable excitable regimes that are influenced by the combination of stochastic variability in forcings and internal feedbacks. In these regimes, the characteristics of individual events are primarily controlled by the system dynamics, whereas the interval between events is determined

by the combination of external stochastic forcing and the size of stability threshold. The controls in these regimes are therefore different from those in stable regimes (where the system response is approximately proportional to the external trigger, and individual events are directly related to external forcings) and in oscillatory regimes (where the oscillation period is determined by the system dynamics alone). The excitable system response may result from small perturbations that leave little or no trace in the geochemical record, and is also a generic result of small changes in any tectonic, climate or ecological forcings that are sufficient to move the system out of a local domain of stability. A statistical approach may then be required to test hypotheses, comparing event probabilities to predicted stability.

Model limitations and future work

The approach we have developed here combines dynamical systems theory with a hierarchy of biogeochemical models to provide a robust framework on which future work can build, including: (i) extending to include additional processes and biogeochemical proxies; (ii) combining multi-proxy spatially-resolved datasets with dynamical constraints to test process-based hypotheses; and (iii) testing hypotheses for the interactions between tectonic and other forcings and system dynamics.

We have not addressed here the evolutionary and tectonic processes that drive long-timescale secular evolution over Earth history. This will require including long-timescale sedimentary reservoirs for carbon and sulphur (*73*), as well as representing changes in metamorphic and degassing fluxes (*5*) and evolution of the marine (*26, 28*) and terrestrial (*34*) biota and vegetation. A spatially-explicit representation of weathering and burial fluxes averaged over short climate or ocean-circulation timescales, including both biotic and paleogeographic controls on land weathering fluxes (*71, 72*) and marine productivity and burial fluxes (*24, 74, 75*) will be required to distinguish process controls from generic properties of long-timescale dynamics.

This will also enable improved process representation of globally-averaged proxy systems such as uranium and molybdenum isotopes (as well as tracers of ocean redox structure such as I/Ca), and is fundamentally required to represent local redox proxies such as iron speciation (*6*).

We identify several targets for ongoing and future work. Hypotheses for the interactions between small "stochastic" forcings (including sea level change affecting both shelf area available for burial fluxes and weathering inputs, and LIP and metamorphic CO_2 inputs) and internal feedbacks in the marginally (un)stable excitable regime can be tested against multi-proxy datasets with updated Neoproterozoic to early Paleozoic stratigraphic frameworks (*19*). The combined effect and relative contribution of (local) diagenetic and spatial controls on the redox sensitivity of globally integrated marine organic carbon and phosphorus burial can be elucidated by combining spatially resolved models for the marine environment, process models for early diagenesis, and phosphorus speciation data (*76*). Including a Phanerozoic terrestrial biota (hence land organic carbon burial and fire feedback regulation of atmospheric oxygen) in a dynamical systems framework can address the underlying controls on Phanerozoic trends in the carbon isotope record and OAE (*cf.* (*15, 20*)), from excitation of OAE by phosphorus inputs from Paleozoic early land plant weathering as a hypothesis for Silurian positive carbon isotope events, to the apparent stability and remarkably limited marine anoxia characteristic of Cenozoic hyperthermals. Including the sulfur system (*73*), a more representative climate system, and the oxidation of additional organic carbon pools, can address the dynamics of global glaciations in the Cryogenian and the most extreme negative carbon isotope fluctuations.

Methods

Model overview

We partition the Earth system into a subset (the ocean, atmosphere, land surface) represented explicitly as a dynamical system by a coupled system of ordinary differential equations (ODEs),

and a subset (including tectonic inputs and controls on weathering and paleogeography) represented only by parameters and forcing terms. We then construct a model that includes biogeochemical reservoirs for atmosphere-ocean phosphorus, carbon and oxygen and explicit hypotheses for the processes and feedbacks that control them, and exploit timescale separation to analyse the coupled system dynamics and stability.

Biogeochemical model

We represent the long-timescale ($10^5 - 10^7$ yr) evolution of atmosphere-ocean carbon A, oxygen O, and marine phosphorus P reservoirs using a system of coupled ODEs, Fig. 2. We describe the overall structure of the equations below and the functional forms in the Supplementary Materials. We use previous formulations (based on the GEOCARB (*44*) and COPSE models, (*33, 77*)) for the land surface weathering functions appropriate for a pre-land-plant world, and combine these with a spatially explicit approach to marine burial fluxes.

The time evolution of ocean phosphorus P is determined by the weathering source $F_{P\_w}(O, A)$ and ocean-integrated burial sink $F_{P\_b}(O, P)$:

$$\frac{dP}{dt} = F_{P\_w}(O, A) - F_{P\_b}(O, P) \tag{1}$$

The time evolution of atmosphere-ocean oxygen O is controlled by the balance between the net oxygen source from organic carbon burial $F_{Corg\_b}(O, P)$, oxygen-sensitive land-surface oxidative weathering $k_{ox}(O/O_0)^{0.5}$, and tectonic reductant input $k_{red}F_{degass}$ (where $k_{red} \approx 0.25$) (*33, 44*):

$$\frac{dO}{dt} = F_{Corg\_b}(O, P) - k_{ox}(O/O_0)^{0.5} - k_{red}F_{degass} \tag{2}$$

Atmosphere-ocean carbon A is controlled by the balance between degassing F_{degass}, carbonate weathering $F_{Ccarb\_w}(A)$ and organic carbon oxidative weathering inputs, and organic and carbonate burial outputs $F_{Corg\_b}(O, P)$, F_{Ccarb_b},

$$\frac{dA}{dt} = k_{ox}(O/O_0)^{0.5} - F_{S\_w}(A) - F_{Corg\_b}(O,P) + F_{degass} \quad (3)$$

where we assume instantaneous alkalinity balance and hence that $F_{Ccarb\_b} = F_{Ccarb\_w}(A) + F_{S\_w}(A)$ where $F_{S\_w}(A)$ is silicate weathering.

The timescales for each reservoir can be estimated as the ratio of typical Neoproterozoic reservoir content (mol) to flux ($\mathrm{mol\,yr^{-1}}$) (Supplementary Materials Table *S2*): phosphorus P $\tau_P \approx 3 \times 10^{15}/4 \times 10^{10} \approx 10^5\,\mathrm{yr}$; atmosphere-ocean carbon A $\tau_A \approx \sqrt{(10)} \times 3 \times 10^{18}/7.9 \times 10^{12} \approx 10^6\,\mathrm{yr}$ (assuming $p\mathrm{CO}_2 \approx 10\times$ modern value); and oxygen O $\tau_O \approx 0.5 \times 3.7 \times 10^{19}/4.5 \times 10^{12} \approx 4 \times 10^6\,\mathrm{yr}$ (assuming 0.5 PAL).

The biogeochemical model represents long-timescale ($10^4 - 10^8\,\mathrm{yr}$) evolution of atmosphere-ocean carbon (A), oxygen (O) and marine phosphorus (P) reservoirs using a system of coupled ODE. Solar luminosity is held fixed at value appropriate to 600 Ma.

Idealized ocean column model

The column model (Fig. 2B) is employed as an abstracted representation of the distribution of burial fluxes across heterogeneous oceanfloor redox environments. It represents the global ocean as a set of columns, where water column oxygen demand varies between columns controlled by per-column parameters k_U^i (the oxygen utilization). We assume that marine export production in each column is proportional to global marine phosphorus P, and that water column oxygen demand and organic carbon burial F_{corg}^i are proportional to export production and hence P. Ocean floor oxygen in column i is then given by the balance between oxygen supply (proportional to atmospheric oxygen) and demand as

$$O_{floor}^i/O_0 = O/O_0 - k_U^i(P/P_0) \quad (4)$$

Phosphorus burial F_{Pb}^i is proportional to export production and with a potential sensitivity to local ocean floor oxygen level O_{floor}^i defined by an oxygen-sensitive C:P burial ratio $CP_{burial}(O_{floor}^i)$

(Supplementary Materials Eq. S11) where we initially make the simplifying assumption that this is close to a step function at zero oxygen and explore the effect of a progressive transition in sensitivity studies (Supplementary Materials Fig. S12). Ordering columns by increasing k_U (decreasing O_{floor}), the relevant control on ocean-integrated burial of organic carbon and phosphorus can be represented by considering k_U as a function of normalized cumulative organic carbon burial C_{org_cuml}, where we use a linear parameterisation of $k_U(C_{org\_cuml})$ (Fig. 3, Supplementary Materials Eq. S13) to explore the effect of spatial heterogeneity on globally integrated phosphorus burial.

Intermediate-complexity ocean model

The intermediate-complexity ocean biogeochemical model is based on the physical circulation from the 79-box global ocean model of Romaniello & Derry (2010) (*78*), extended here with a catalog of ocean shelf configurations (Supplementary Materials Fig. S2, S3). The pelagic ocean is represented by two columns for low and high latitudes, with a third column representing upwelling margins. The shelf catalog consists of 21 2-box shelves, with ocean connectivity at varying depths from surface to 1000m generating a range of shelf nutrient levels, and shelf area configurable to represent different paleogeographic configurations. The biogeochemical model includes two tracers for ocean oxygen and phosphorus, air-sea exchange of oxygen, a restoring-based parameterisation of export production, a Martin power-law parameterization for the biological pump, and a burial-efficiency parameterisation for organic carbon and phosphorus burial. Global marine burial fluxes are tabulated across a grid of atmospheric oxygen and total marine phosphorus levels by time-integrating the ocean model to steady-state, and shelf areas are adjusted to generate the prescribed distributions of burial fluxes across redox environments shown in Fig. 2 and 3 and Supplementary Materials Fig. S4. For full details see the Supplementary Materials.

Stability and oscillation timescale near the neutrally stable limit

The stability and oscillation rate near the neutrally-stable limit (the "hysteresis bifurcation" of the critical manifold, where the critical manifold is parallel to the fast fibres) can be derived from linear stability analysis (see eg (*55*)). In the singular limit (where the ratio of timescales is very large), the hysteresis bifurcation separates a globally stable regime from a limit-cycle regime. When the separation of timescales is finite, both the stability criteria and the oscillation timescale are modified. We show in Supplementary Materials Fig. S5 numerical experiments illustrating the change in oscillation period across the hysteresis bifurcation in the critical manifold for the P-O model, including an example of the damped oscillation in the neutrally-stable limit.

The oscillation timescale and stability criteria in the non-singular case (with finite timescale separation) can be derived using linear stability analysis. Although the analysis is general, we consider here the phosphorus-oxygen two-state-variable system, with time evolution of the fast variable P and slow variable O given by:

$$\frac{d}{dt}\begin{pmatrix} P \\ O \end{pmatrix} = \begin{pmatrix} f_P(P,O) \\ f_O(P,O) \end{pmatrix} \tag{5}$$

Linearizing about an equilibrium point P_0, O_0 so $P = P_0 + \Delta P$ and $O = O_0 + \Delta O$, we have:

$$\frac{d}{dt}\begin{pmatrix} \Delta P \\ \Delta O \end{pmatrix} = \begin{pmatrix} \left(\frac{\partial f_P}{\partial P}\right)_O & \left(\frac{\partial f_P}{\partial O}\right)_P \\ \left(\frac{\partial f_O}{\partial P}\right)_O & \left(\frac{\partial f_O}{\partial O}\right)_P \end{pmatrix} \begin{pmatrix} \Delta P \\ \Delta O \end{pmatrix} \tag{6}$$

The Jacobian terms are $\approx 1/\tau$ where τ is a timescale, hence this is approximately:

$$\frac{d}{dt}\begin{pmatrix} \Delta P \\ \Delta O \end{pmatrix} \approx \begin{pmatrix} \alpha/\tau_P & -1/\tau_P \\ +1/\tau_O & -1/\tau_O \end{pmatrix} \begin{pmatrix} \Delta P \\ \Delta O \end{pmatrix} \tag{7}$$

Here we have assumed that we are close to the hysteresis bifurcation, hence the critical manifold is nearly parallel to the fast fibers so that the P restoring term $(\frac{\partial f_P}{\partial P}) \approx \alpha/\tau_P$ where α is the (small) angle between the critical manifold and the fast fibres.

The stability and oscillation timescale then follow from the eigenvalues which are:

$$\lambda = \frac{1}{2}\left(\frac{\alpha}{\tau_P} - \frac{1}{\tau_O}\right) \pm \sqrt{\frac{1}{4}\left(\frac{1}{\tau_O} - \frac{\alpha}{\tau_P}\right)^2 - \frac{1}{\tau_P\,\tau_O}} \tag{8}$$

Assuming $\tau_O \gg \tau_P$ this then shows that

$$\lambda \approx \frac{1}{2}\left(\frac{\alpha}{\tau_P} - \frac{1}{\tau_O}\right) \pm i(\tau_P\,\tau_O)^{-0.5} \tag{9}$$

At the hysteresis bifurcation (when $\alpha = 0$), this is a damped oscillation with period $\approx (\tau_P\,\tau_O)^{0.5}$ and decay timescale $\approx \tau_O$. The marginally-stable case where the real part of the eigenvalue is zero then corresponds to $\alpha \approx \tau_P/\tau_O$. If $\epsilon = \tau_P/\tau_O$ is the ratio of timescales, in the singular limit where $\epsilon \to 0$ the oscillation period $\epsilon^{0.5}\tau_O$ tends to zero as the hysteresis bifurcation is approached and the stability boundary $\alpha \approx \epsilon$ approaches the hysteresis bifurcation at $\alpha = 0$. Finite timescale separation results in a small stabilising term (so oscillations at the hysteresis bifurcation are damped, and stability is maintained up to a small value of α) and a limiting value of the oscillation period (where this limiting value represents the fastest possible limit cycle oscillation).

For the phosphorus-oxygen model, the oscillation period in the neutrally stable limit (and hence the fastest possible limit cycle oscillation) is then $\approx (\tau_P\tau_O)^{0.5}$ ie the geometrical mean of the phosphorus timescale τ_P and oxygen timescale τ_O. The decay time for the damped oscillation in the neutrally stable case is $\approx \tau_O$.

For the phosphorus-carbon-oxygen model, assuming that the limit-cycle oscillations near the hysteresis bifurcation do not involve any slow oxygen-timescale segments, the same analysis shows how the limiting oscillation period and modified stability criteria depend on the ratio of the phosphorus and carbon timescales.

Stochastic forcing

We illustrate the effect of a generic small stochastic forcing on the system dynamics by adding a white-noise term to the differential equation for the A reservoir (Eq. 3), where physically this represents a stochastic variation in the degassing input F_{degass}:

$$\frac{dA}{dt} = k_{ox}(O/O_0)^{0.5} - F_{S\_w}(A) - F_{Corg\_b}(O,P) + F_{degass} + D\xi(t) \tag{10}$$

The parameter D governs the amplitude of the applied stochastic forcing defined by the standard white noise $\xi(t)$, where $D = 9.6 \times 10^{14}\,\mathrm{mol\,yr^{-0.5}}$ to give normally-distributed fluctuations with expectation $0.96 \times 10^{12}\,\mathrm{mol\,yr^{-1}}$ when averaged over $10^6\,\mathrm{yr}$ intervals. See Supplementary Materials for details of the numerical method used to integrate the resulting system of stochastic differential equations (Eq. 1, 2, 10).

Sensitivity studies

To establish whether these results are robust to known uncertainties in model parameters we performed sensitivity studies relative to the baseline case shown in Fig. 5 across the ranges considered in the COPSE (*33*) and COPSE reloaded (*77*) models. Reducing the organic carbon cycle size (Supplementary Materials Fig. S10) with a reduction in modern marine organic carbon burial from 4.5×10^{12} to $2.5 \times 10^{12}\,\mathrm{mol\,yr^{-1}}$ increases the oscillation period by a factor of about two (*i.e.* consistent with the reduced organic carbon flux) but produces a smaller reduction in the magnitude of the $\delta^{13}\mathrm{C}$ excursion. Reducing the magnitude of the oxic-anoxic change in Corg:P burial ratio to a factor of 2 (Supplementary Materials Fig. S13) reduces the magnitude of the change in marine phosphorus, and hence in marine organic carbon burial and the amplitude of the $\delta^{13}\mathrm{C}$ excursion, does not significantly change the limit cycle behaviour, and reduces the oscillation period by a factor of $\approx 2/3$. Higher degassing and silicate weathering, or a smaller organic carbon cycle (Supplementary Materials Fig. S11, S10), "flattens" the A

nullcline, as the organic carbon cycle has less influence on atmosphere-ocean carbon, reducing the amplitude of the excursion in A and hence CO_2, increasing the amplitude of the excursion in oxygen, and reducing the region of parameter space where fast phosphorus-carbon oscillations would be possible (compare Fig. 10, Supplementary Materials Fig. S10). Modifying the local redox dependence of Corg:P burial ratio so that this occurs over a range in oceanfloor oxygen can produces a similar effect on globally-integrated phosphorus burial to broadening the range of oceanfloor redox environments over which burial is distributed (Supplementary Materials Fig. S12). Modifying the partitioning of phosphorus weathering between fractions that scale with silicate, carbonate and oxidative weathering rates (Supplementary Materials Fig. S9) demonstrates that the phase plane nullclines and hence limit cycle are relatively insensitive to partitioning between silicate and carbonate weathering (as the temperature and CO_2 dependence are not greatly different); that the baseline silicate-weathering-only configuration is very similar to the COPSE reloaded silicate-dominated case; and that although including a fraction 0.4 of phosphorus weathering that scales as oxidative weathering changes the shape of the critical manifold, this is handled consistently by the GSPT approach and also doesn't qualitatively change the limit cycle regime.

Model configurations

Full details of the parameters used for all model configurations are shown in Supplementary Materials Table S4.

Numerical methods and code availability

Models were implemented in the Julia programming language (*79*) using the open-source PALEOtoolkit framework (*80*); see Supplementary Materials for Julia packages used. Additional model configurations and components specific to this study are available on request and will be

made available in a public github code repository upon publication.

Acknowledgements

Funding

S.J.D was supported by National Environment Research Council grant NE/T008458/1. Z.H.L. was supported by the programs of China Scholarships Council (No. 202106410094)

Author contributions

Conceptualization: S.J.D, Methodology: S.J.D, Z.H.L, Investigation: Z.H.L, S.J.D, Visualization: Z.H.L, Writing—original draft: S.J.D, Writing—review & editing: S.J.D, Z.H.L.

Competing interests

The authors declare that they have no competing interests.

Data and materials availability

All model codes will be made available in a public github code repository upon publication.

References

1. E Turner, A Bekker, Thick sulfate evaporite accumulations marking a mid-Neoproterozoic oxygenation event (Ten Stone Formation, Northwest Territories, Canada). *Geological Society of America Bulletin* p. B31268.1 (2015).

2. JK Prince, RH Rainbird, BA Wing, Evaporite deposition in the mid-Neoproterozoic as a driver for changes in seawater chemistry and the biogeochemical cycle of sulfur. *Geology* **47**, 375–379 (2019).

3. IJ Glasspool, AC Scott, Phanerozoic concentrations of atmospheric oxygen reconstructed from sedimentary charcoal. *Nature Geoscience* **3**, 627–630 (2010) Publisher: Nature Publishing Group.

4. MW Wallace, et al., Oxygenation history of the Neoproterozoic to early Phanerozoic and the rise of land plants. *Earth and Planetary Science Letters* **466**, 12–19 (2017) ISBN: 0012-821X Publisher: Elsevier B.V.

5. AJ Krause, BJW Mills, AS Merdith, TM Lenton, SW Poulton, Extreme variability in atmospheric oxygen levels in the late Precambrian. *Science Advances* **8**, eabm8191 (2022).

6. EA Sperling, et al., Statistical analysis of iron geochemical data suggests limited late Proterozoic oxygenation. *Nature* **523**, 451–454 (2015) ISBN: 0028-0836.

7. SK Sahoo, et al., Oceanic oxygenation events in the anoxic Ediacaran ocean. *Geobiology* **14**, 457–468 (2016).

8. KV Lau, FA Macdonald, K Maher, JL Payne, Uranium isotope evidence for temporary ocean oxygenation in the aftermath of the Sturtian Snowball Earth. *Earth and Planetary Science Letters* **458**, 282–292 (2017) Publisher: Elsevier B.V.

9. R Tostevin, et al., Uranium isotope evidence for an expansion of anoxia in terminal Ediacaran oceans. *Earth and Planetary Science Letters* **506**, 104–112 (2019).

10. GY Wei, et al., Global marine redox evolution from the late Neoproterozoic to the early Paleozoic constrained by the integration of Mo and U isotope records. *Earth-Science Reviews* **214**, 103506 (2021).

11. F Zhang, et al., Global marine redox changes drove the rise and fall of the Ediacara biota. *Geobiology* **17**, 594–610 (2019).

12. TW Dahl, et al., Atmosphere–ocean oxygen and productivity dynamics during early animal radiations. *Proceedings of the National Academy of Sciences* **116**, 19352–19361 (2019).

13. T He, et al., Possible links between extreme oxygen perturbations and the Cambrian radiation of animals. *Nature Geoscience* **12**, 468–474 (2019).

14. TW Dahl, et al., Uranium isotopes distinguish two geochemically distinct stages during the later Cambrian SPICE event. *Earth and Planetary Science Letters* **401**, 313–326 (2014) Publisher: Elsevier B.V.

15. T Reershemius, NJ Planavsky, What controls the duration and intensity of ocean anoxic events in the Paleozoic and the Mesozoic? *Earth-Science Reviews* **221**, 103787 (2021).

16. R Bartlett, et al., Abrupt global-ocean anoxia during the Late Ordovician–early Silurian detected using uranium isotopes of marine carbonates. *Proceedings of the National Academy of Sciences* **115**, 5896–5901 (2018).

17. C Zou, et al., Ocean euxinia and climate change "double whammy" drove the Late Ordovician mass extinction. *Geology* **46**, 535–538 (2018).

18. B Cramer, I Jarvis, Carbon Isotope Stratigraphy in *Geologic Time Scale 2020*. (Elsevier), pp. 309–343 (2020).

19. FT Bowyer, et al., Calibrating the temporal and spatial dynamics of the Ediacaran - Cambrian radiation of animals. *Earth-Science Reviews* **225**, 103913 (2022).

20. A Bachan, et al., A model for the decrease in amplitude of carbon isotope excursions across the Phanerozoic. *American Journal of Science* **317**, 641–676 (2017).

21. S Xiao, et al., Biostratigraphic and chemostratigraphic constraints on the age of early Neoproterozoic carbonate successions in North China. *Precambrian Research* **246**, 208–225 (2014).

22. EA Sperling, et al., Oxygen, ecology, and the Cambrian radiation of animals. *Proceedings of the National Academy of Sciences of the United States of America* **110**, 13446–51 (2013).

23. SA Darroch, EF Smith, M Laflamme, DH Erwin, Ediacaran Extinction and Cambrian Explosion. *Trends in Ecology & Evolution* **33**, 653–663 (2018).

24. F Bowyer, RA Wood, SW Poulton, Controls on the evolution of Ediacaran metazoan ecosystems: A redox perspective. *Geobiology* **15**, 516–551 (2017) ISBN: 1472-4669 (Electronic) 1472-4669 (Linking).

25. R Wood, et al., Integrated records of environmental change and evolution challenge the Cambrian Explosion. *Nature Ecology & Evolution* **3**, 528–538 (2019).

26. GA Logan, JM Hayes, GB Hieshima, RE Summons, Terminal Proterozoic reorganization of biogeochemical cycles. *Nature* **376**, 53–56 (1995) Publisher: Nature Publishing Group.

27. TM Lenton, RA Boyle, SW Poulton, GA Shields-zhou, NJ Butterfield, Co-evolution of eukaryotes and ocean oxygenation in the Neoproterozoic era. *Nature Geoscience* **7**, 257–265 (2014).

28. Ra Boyle, et al., Stabilization of the coupled oxygen and phosphorus cycles by the evolution of bioturbation. *Nature Geoscience* **7**, 671–676 (2014).

29. TM Lenton, SJ Daines, The effects of marine eukaryote evolution on phosphorus, carbon and oxygen cycling across the Proterozoic–Phanerozoic transition. *Emerging Topics in Life Sciences* **2**, 267–278 (2018).

30. LR Kump, Biogeochemical cycle of oxygen in *Encyclopedia of Earth System Science, Vol. 3*, ed. WA Nierenberg. (Academic Press, NY), (1991).

31. LJ Alcott, BJW Mills, SW Poulton, Stepwise Earth oxygenation is an inherent property of global biogeochemical cycling. *Science* **366**, 1333–1337 (2019).

32. SJ Daines, BJW Mills, TM Lenton, Atmospheric oxygen regulation at low Proterozoic levels by incomplete oxidative weathering of sedimentary organic carbon. *Nature Communications* **8**, 14379 (2017).

33. NM Bergman, TM Lenton, AJ Watson, COPSE: A new model of biogeochemical cycling over phanerozoic time. *American Journal of Science* **304**, 397–437 (2004).

34. TM Lenton, et al., Earliest land plants created modern levels of atmospheric oxygen. *Proceedings of the National Academy of Sciences* **113**, 9704–9709 (2016).

35. LR Kump, Terrestrial feedback in atmospheric oxygen regulation by fire and phosphorus. *Nature* **335**, 152–154 (1988).

36. TM Lenton, AJ Watson, Redfield revisited: 2. What regulates the oxygen content of the atmosphere? *Global Biogeochemical Cycles* **14**, 249–268 (2000) Publisher: American Geophysical Union.

37. P Van Cappellen, ED Ingall, Benthic phosphorus regeneration, net primary production, and ocean anoxia: A model of the coupled marine biogeochemical cycles of carbon and phosphorus. *Paleoceanography* **9**, 677 (1994).

38. P Van Cappellen, ED Ingall, Redox Stabilization of the Atmosphere and Oceans by Phosphorus-Limited Marine Productivity. *Science* **271**, 493–496 (1996).

39. IC Handoh, TM Lenton, Periodic mid-Cretaceous oceanic anoxic events linked by oscillations of the phosphorus and oxygen biogeochemical cycles. *Global Biogeochemical Cycles* **17**, 1–11 (2003).

40. CW Arnscheidt, DH Rothman, The Balance of Nature: A Global Marine Perspective. *Annual Review of Marine Science* **14**, 49–73 (2022).

41. JC Walker, P Hays, JF Kasting, A negative feedback mechanism for the long-term stabilization of the Earth's surface temperature. *Journal of Geophysical Research* **86**, 9776–9782 (1981).

42. T Tyrrell, The relative influences of nitrogen and phosphorus on oceanic primary production. *Nature* **400**, 525–531 (1999).

43. AJ Watson, JE Lovelock, Biological homeostasis of the global environment: the parable of Daisyworld. *Tellus B* **35**, 284–289 (1983) Publisher: Wiley Online Library.

44. RA Berner, GEOCARB II; a revised model of atmospheric CO 2 over Phanerozoic time. *American Journal of Science* **294**, 56–91 (1994).

45. DH Rothman, Characteristic disruptions of an excitable carbon cycle. *Proceedings of the National Academy of Sciences* (2019).

46. CW Arnscheidt, DH Rothman, Routes to global glaciation. *Proceedings of the Royal Society A: Mathematical, Physical and Engineering Sciences* **476**, 20200303 (2020).

47. R FitzHugh, Mathematical models of threshold phenomena in the nerve membrane. *The Bulletin of Mathematical Biophysics* **17**, 257–278 (1955).

48. EM Izhikevich, *Dynamical systems in neuroscience: the geometry of excitability and bursting*, Computational neuroscience. (MIT press, Cambridge, Mass), (2007).

49. AS Pikovsky, J Kurths, Coherence Resonance in a Noise-Driven Excitable System. *Physical Review Letters* **78**, 775–778 (1997).

50. RE Lee DeVille, E Vanden-Eijnden, CB Muratov, Two distinct mechanisms of coherence in randomly perturbed dynamical systems. *Physical Review E* **72**, 031105 (2005).

51. S Wieczorek, P Ashwin, CM Luke, PM Cox, Excitability in ramped systems: the compost-bomb instability. *Proceedings of the Royal Society A: Mathematical, Physical and Engineering Sciences* **467**, 1243–1269 (2011).

52. P Ashwin, S Wieczorek, R Vitolo, P Cox, Tipping points in open systems: bifurcation, noise-induced and rate-dependent examples in the climate system. *Philosophical Transactions of the Royal Society A: Mathematical, Physical and Engineering Sciences* **370**, 1166–1184 (2012).

53. A Lesne, Multiscale Approaches in *Encyclopedia of Mathematical Physics*. (Elsevier), pp. 465–482 (2006).

54. PG Kevrekidis, et al., Equation-Free, Coarse-Grained Multiscale Computation: Enabling Mocroscopic Simulators to Perform System-Level Analysis. *Communications in Mathematical Sciences* **1**, 715–762 (2003) _eprint: 0209043.

55. SH Strogatz, *Nonlinear dynamics and chaos: with applications to physics, biology, chemistry, and engineering*, Studies in nonlinearity. (Addison-Wesley publ, Reading (Mass.)), (1994).

56. C Kuehn, *Multiple Time Scale Dynamics*, Applied Mathematical Sciences. (Springer International Publishing, Cham) Vol. 191, (2015).

57. M Wechselberger, *Geometric Singular Perturbation Theory Beyond the Standard Form*, Frontiers in Applied Dynamical Systems: Reviews and Tutorials. (Springer International Publishing, Cham) Vol. 6, (2020).

58. KHM Nyman, P Ashwin, PD Ditlevsen, Bifurcation of critical sets and relaxation oscillations in singular fast-slow systems. *Nonlinearity* **33**, 2853–2904 (2020).

59. CP Slomp, P Van Cappellen, The global marine phosphorus cycle: sensitivity to oceanic circulation. *Biogeosciences* **4**, 155–171 (2007).

60. ED Ingall, RM Bustin, PVAN Cappellen, Influence of water column anoxia on the burial and preservation of carbon and phosphorus in marine shales. *Geochimica et Cosmochimica Acta* **57**, 303–316 (1993).

61. TJ Algeo, ED Ingall, Sedimentary Corg:P ratios, paleocean ventilation, and Phanerozoic atmospheric pO2. *Palaeogeography, Palaeoclimatology, Palaeoecology* **256**, 130–155 (2007).

62. CP Slomp, J Thomson, GJ De Lange, Controls on phosphorus regeneration and burial during formation of eastern Mediterranean sapropels. *Marine Geology* **203**, 141–159 (2004).

63. AW Dale, RA Boyle, TM Lenton, ED Ingall, K Wallmann, A model for microbial phosphorus cycling in bioturbated marine sediments: Significance for phosphorus burial in the early Paleozoic. *Geochimica et Cosmochimica Acta* **189**, 251–268 (2016).

64. M Zhao, S Zhang, LG Tarhan, CT Reinhard, N Planavsky, The role of calcium in regulating marine phosphorus burial and atmospheric oxygenation. *Nature Communications* **11**, 2232 (2020).

65. IV Tsandev, CP Slomp, Modeling phosphorus cycling and carbon burial during Cretaceous Oceanic Anoxic Events. *Earth and Planetary Science Letters* **286**, 71–79 (2009) Publisher: Elsevier B.V.

66. R Ernst, M Wingate, K Buchan, Z Li, Global record of 1600–700Ma Large Igneous Provinces (LIPs): Implications for the reconstruction of the proposed Nuna (Columbia) and Rodinia supercontinents. *Precambrian Research* **160**, 159–178 (2008).

67. TJ Algeo, SE Scheckler, Terrestrial-marine teleconnections in the Devonian: links between the evolution of land plants, weathering processes, and marine anoxic events. *Philosophical Transactions of the Royal Society B: Biological Sciences* **353**, 113–130 (1998).

68. AJ Watson, TM Lenton, BJW Mills, Ocean deoxygenation, the global phosphorus cycle and the possibility of human-caused large-scale ocean anoxia. *Philosophical Transactions of the Royal Society A: Mathematical, Physical and Engineering Sciences* **375**, 20160318 (2017).

69. O Lehnert, P Männik, MM Joachimski, M Calner, J Frýda, Palaeoclimate perturbations before the Sheinwoodian glaciation: A trigger for extinctions during the 'Ireviken Event'. *Palaeogeography, Palaeoclimatology, Palaeoecology* **296**, 320–331 (2010).

70. J Krissansen-Totton, MA Kipp, DC Catling, Carbon cycle inverse modeling suggests large changes in fractional organic burial are consistent with the carbon isotope record and may have contributed to the rise of oxygen. *Geobiology* **19**, 342–363 (2021).

71. Y Goddéris, Y Donnadieu, G Le Hir, V Lefebvre, E Nardin, The role of palaeogeography in the Phanerozoic history of atmospheric CO2 and climate. *Earth-Science Reviews* **128**, 122–138 (2014) Publisher: Elsevier B.V.

72. BJ Mills, Y Donnadieu, Y Goddéris, Spatial continuous integration of Phanerozoic global biogeochemistry and climate. *Gondwana Research* **100**, 73–86 (2021).

73. GA Shields, et al., Unique Neoproterozoic carbon isotope excursions sustained by coupled evaporite dissolution and pyrite burial. *Nature Geoscience* **12**, 823–827 (2019).

74. J Trabucho Alexandre, et al., The mid-Cretaceous North Atlantic nutrient trap: Black shales and OAEs. *Paleoceanography* **25**, PA4201 (2010).

75. A Pohl, et al., Continental configuration controls ocean oxygenation during the Phanerozoic. *Nature* **608**, 523–527 (2022).

76. Y Xiong, et al., Phosphorus cycling in Lake Cadagno, Switzerland: A low sulfate euxinic ocean analogue. *Geochimica et Cosmochimica Acta* **251**, 116–135 (2019).

77. TM Lenton, SJ Daines, BJ Mills, COPSE reloaded: An improved model of biogeochemical cycling over Phanerozoic time. *Earth-Science Reviews* **178**, 1–28 (2018).

78. SJ Romaniello, LA Derry, An intermediate-complexity model for simulating marine biogeochemistry in deep time: Validation against the modern global ocean. *Geochemistry, Geophysics, Geosystems* **11** (2010).

79. J Bezanson, A Edelman, S Karpinski, VB Shah, Julia: A Fresh Approach to Numerical Computing. *SIAM Review* **59**, 65–98 (2017).

80. SJ Daines, J Eager-Nash, Z Li, S Sjosten, X Chen, PALEOtoolkit (2023) `https://github.com/PALEOtoolkit`.

81. G Hek, Geometric singular perturbation theory in biological practice. *Journal of mathematical biology* **60**, 347–86 (2010).

82. C Rackauckas, Q Nie, DifferentialEquations.jl – A Performant and Feature-Rich Ecosystem for Solving Differential Equations in Julia. *Journal of Open Research Software* **5**, 15 (2017).

83. AC Hindmarsh, et al., SUNDIALS: Suite of nonlinear and differential/algebraic equation solvers. *ACM Transactions on Mathematical Software* **31**, 363–396 (2005).

84. C Rackauckas, Q Nie, Adaptive methods for stochastic differential equations via natural embeddings and rejection sampling with memory. *Discrete and continuous dynamical systems. Series B* **22**, 2731 (2017).

85. J Revels, M Lubin, T Papamarkou, Forward-Mode Automatic Differentiation in Julia (2016) arXiv:1607.07892 [cs].

86. S Danisch, J Krumbiegel, Makie.jl: Flexible high-performance data visualization for Julia. *Journal of Open Source Software* **6**, 3349 (2021).

87. JL Sarmiento, N Gruber, *Ocean biogeochemical dynamics*. (Princeton University Press, Princeton), (2006) OCLC: ocm60651167.

88. R Wanninkhof, Relationship Between Wind Speed and Gas Exchange Over the Ocean. *Journal of Geophysical Research* **97**, 7373–7382 (1992).

89. JH Martin, GA Knauer, DM Karl, WW Broenkow, VERTEX: carbon cycling in the northeast Pacific. *Deep Sea Research Part A, Oceanographic Research Papers* **34**, 267–285 (1987).

90. K Ozaki, S Tajima, E Tajika, Conditions required for oceanic anoxia/euxinia: Constraints from a one-dimensional ocean biogeochemical cycle model. *Earth and Planetary Science Letters* **304**, 270–279 (2011).

91. SM Henrichs, WS Reeburgh, Anaerobic mineralization of marine sediment organic matter: Rates and the role of anaerobic processes in the oceanic carbon economy. *Geomicrobiology Journal* **5**, 191–237 (1987).

92. TK Tromp, P Van Cappellen, RM Key, A global model for the early diagenesis of organic carbon and organic phosphorus in marine sediments. *Geochimica et Cosmochimica Acta* **59**, 1259–1284 (1995).

93. A Olsen, et al., GLODAPv2.2019 – an update of GLODAPv2, (Chemical oceanography), preprint (2019).

Supplementary Materials for

Excitable Dynamics of Neoproterozoic to Early Paleozoic Atmospheric and Ocean Oxygen

Stuart Daines*, Ziheng Li*

*Corresponding author. Email: s.daines@exeter.ac.uk, zihengli@cug.edu.cn

This PDF file includes:

Supplementary Text
Figs. S1 to S14
Tables S1 to S3
Legend for Table S4
References (81 to 93)

Other Supplementary Materials for this manuscript include the following:

Table S4

Supplementary text

Geometric singular perturbation theory (GSPT)

To illustrate the basic ideas of Geometric Singular Perturbation Theory (GSPT) (57, 81) we reproduce the standard analysis for a singularly-perturbed system of ODEs with two different timescales: t the fast, and $\tau = \epsilon t$ the slow, where ϵ is a small parameter ($0 < \epsilon \ll 1$) which gives the system a singular character. Assuming the system is in normal form (where u are fast variables and v are slow variables), the ODEs are of the form

$$\frac{du}{dt} = f(u, v, \epsilon) \quad [S1]$$

$$\frac{dv}{dt} = \epsilon g(u, v, \epsilon) \quad [S2]$$

where $u \in \mathbb{R}^n$ and $v \in \mathbb{R}^m$, $f : \mathbb{R}^{n+m} \to \mathbb{R}^n$, $g : \mathbb{R}^{n+m} \to \mathbb{R}^m$, and f, g are assumed to be sufficiently smooth. With a change in the time scale, the ODEs can be reformulated ($d\tau/dt = \epsilon, du/dt = \epsilon du/d\tau$) as

$$\epsilon \frac{du}{d\tau} = f(u, v, \epsilon) \quad [S3]$$

$$\frac{dv}{d\tau} = g(u, v, \epsilon) \quad [S4]$$

Thus, the Eqns. (S1), (S2) are called the *fast system* and Eqns. (S3), (S4) the *slow system*. They are equivalent as long as the $\epsilon \neq 0$. When we set a limit as $\epsilon \to 0$ the fast system reduces to the *layer problem*:

$$\frac{du}{dt} = f(u, v, 0) \quad [S5]$$

$$\frac{dv}{dt} = 0 \quad [S6]$$

and the slow system to the *reduced problem*:

$$0 = f(u, v, 0) \quad [S7]$$

$$\frac{dv}{d\tau} = g(u, v, 0) \quad [S8]$$

The two limits are two different approximations of the full $\epsilon > 0$ system. The Eqns. (S5), (S6) for the layer problem show that the slow variables v are constant on the timescale t (Eq. S6), with the fast variables u evolving along *fast fibres* according to Eq. (S5). The reduced Eqns. (S7), (S8) for the slow system show that this system describes a flow along the m-dimensional *critical manifold* defined by Eq. (S7).

The main idea of GSPT is that there exists a *slow manifold* with $\epsilon \neq 0$, which has the critical manifold as its leading order approximation. The analysis above in the limit $\epsilon \to 0$ then provides a first approximation to the dynamics of the full system: in phase space, the system moves rapidly (timescale t) from its starting position along a fast fibre until it reaches and moves along the slow manifold, which to leading order is described by the flow (timescale τ) on the critical manifold. The goal of GSPT is to formalize this analysis of the dynamics of fast and slow systems and generalize to nonzero but small ϵ by suitably combining the dynamics of these two limits (57, 81), using a geometric approach that is not restricted to the normal form shown here. This concept of the slow manifold generalizes older results about center manifolds (53).

The critical manifold is attracting where the linearized layer problem has eigenvalue(s) with negative real part, and repelling where it has eigenvalue(s) with positive real part, where these regions are separated by *folds* where an eigenvalue crosses the imaginary axis. In the singular limit, a trajectory will move along a fast fibre (the layer flow, ie fast variables u evolve at constant values of the slow variables v) until it reaches an attracting part of the critical manifold, then follow the slow reduced flow on the critical manifold until it either reaches a steady state or reaches a fold where it will leave the critical manifold and follow a fast fibre. Limit cycle oscillations are then composed of fast and slow segments with switches from fast to slow dynamics at folds. If there is a single fast variable u, the fold criteria (where the eigenvalue for the linearized layer problem changes sign) is $(\partial f(u, v)/\partial u)_v = 0$ (57): this is the criteria used to identify the fold points and lines for the examples shown, where the Jacobian for the numerical model is calculated by automatic differentation.

Numerical methods

Models were implemented in the Julia programming language (79) using the PALEOtoolkit framework (80). Numerical ODE integration was performed using the Julia SciML interface (82) to the SUNDIALS CVODE package (83). Numerical integration of stochastic differential equations was performed using the SOSRA solver from the Julia StochasticDiffEq.jl package (84). Jacobians for fold location and linear stability analysis were calculated using forward-mode automatic differentiation provided by the Julia ForwardDiff.jl package (85). 3D plots were created using the GLMake.jl (86) Julia package.

Biogeochemical Earth system model description

The biogeochemical Earth system model represents the long timescale ($\geq 10^5 - 10^8$yr) evolution of the global atmosphere-ocean carbon A, oxygen O and ocean phosphorus P as a set of coupled ordinary differential equations (main paper Eqns. (1), (2), (3)). There is no explicit representation of sedimentary reservoirs or land biota, hence the model is restricted to timescales shorter than the sedimentary timescales ($\simeq 10^8$yr), and to Earth history prior to the evolution of the land biota at $\simeq 400$ Ma. Model "age" (and hence solar luminosity) is set to a constant mid-Ediacaran value of 600 Ma.

Model functional forms and parameterizations for the atmosphere, climate and land surface are summarized in Table S1, and constants are listed in Table S2. Functional forms and parameterizations are from the GEOCARB (44) and COPSE (33, 77) models. Carbon isotopes are calculated from isotope mass balance for the A reservoir, using the fractionation factors for marine carbonate and organic carbon burial from COPSE (33).

The ocean models are described in the main paper and the following sections: these provide the global marine burial fluxes of phosphorus $F_{P\_b}(O,P)$ and organic carbon $F_{Corg\_b}(O,P)$ (see main paper Eqns. (1), (2), (3)).

Idealized ocean column model description

The column model provides an abstracted representation of the distribution of marine burial fluxes across heterogeneous oceanfloor redox enviroments. It represents the global ocean as a set of columns, where water column oxygen demand varies between columns controlled by per-column parameters k_U^i (the oxygen utilization). We assume that marine export production in each column i is proportional to marine phosphorus P, and that water column oxygen demand and organic carbon burial $mocb^i$ are proportional to export production and hence P.

The globally-integrated marine organic carbon burial flux is then given by the sum over n columns of per-column organic carbon burial $mocb^i$:

$$F_{Corg\_b}(P/P_0) = \sum_1^n mocb^i = \sum_1^n (P/P_0) mocb_0^i = (P/P_0) Corg\_b_0 \quad [S9]$$

where $Corg\_b_0$ is the global marine organic carbon burial flux at normalized phosphorus $(P/P_0) = 1$ and there is no oxygen dependence.

Normalized ocean floor oxygen in column i is then given by the balance between oxygen supply (proportional to atmospheric oxygen) and demand as

$$O^i_{floor}/O_0 = O/O_0 - k_U^i (P/P_0) \quad [S10]$$

where k_U^i is a prescribed per-column oxygen demand that represents spatial variability in ocean-floor redox conditions. Phosphorus burial is linked to local organic carbon burial by an oceanfloor-redox-dependent Corg:P burial ratio CP^i_{burial}. We first define $local\_anoxia^i = 1/(1 + \exp(k_{anox} O^i_{floor}/O_0))$ where for large k_{anox} this is a smoothed step function at $O^i_{floor}/O_0 = 0$. CP^i_{burial} is then parameterized in terms of limiting values for oxic and anoxic conditions CP_{oxic} and CP_{anoxic} as:

$$CP^i_{burial} = \frac{CP_{oxic}\, CP_{anoxic}}{(1 - local\_anoxia^i) * CP_{anoxic} + local\_anoxia^i CP_{oxic}} \quad [S11]$$

This represents a transition from CP_{anoxic} to CP_{oxic} over a range in local oceanfloor oxygen of $\Delta O^i_{floor} \approx O_0/k_{anox}$, where the baseline value $k_{anox} = 100$ provides a sharp transition over a small range in oxygen concentration of $\approx 3\mu$M. The globally-integrated marine phosphorus burial flux is then given by the sum over n columns:

$$F_{P\_b}(O/O_0, P/P_0) = \sum_1^n \frac{mocb^i}{CP^i_{burial}} \quad [S12]$$

Ordering columns by increasing k_U^i (or decreasing O^i_{floor}), the control on ocean-integrated burial of phosphorus can be represented by defining k_U as a function of normalized cumulative organic carbon burial C_{org_cuml}, defined as the sum of organic carbon burial for all columns with lower k_U divided by global marine total organic carbon burial (where given our other assumptions this is just a fixed per-column label, and for convenience in the numerical code we additionally assume a binning into columns with constant organic carbon burial per column so that $C^i_{org\_cuml} = i/n$). We then use a linear parameterisation of $k_U(C_{org\_cuml})$ to explore the effect of spatial heterogeneity on phosphorus and oxygen dynamics:

$$k_U(C_{org\_cuml}) = (1 - C_{org\_cuml})\, k_{O2\_U\_min} + C_{org\_cuml}\, k_{O2\_U\_max} \quad [S13]$$

The positions of the two folds (or changes in slope, if globally stable) in the critical manifold in the P, O phase plane are then controlled by CP_{oxic}, $k_{O2\_U\_max}$ (controlling the location of the fold at low P, where the ocean first develops anoxia), and CP_{anoxic}, $k_{O2\_U\_min}$ (controlling the location of the fold at high P, where the ocean becomes fully anoxic). For example, if the P_{norm} value (the coordinate of the x-axis in P, O phase plane) equals 1.0, we can calculate the coordinate of the folds: (1) the low P fold's = (1.0, 1.0*$k_{O2\_U\_max}$), (2) the high P fold = (1.0*CP_{anoxic}/CP_{oxic}, 1.0*$k_{O2\_U\_min}$*CP_{anoxic}/CP_{oxic}).

We define

$$sharpness = \frac{k_{O2\_U\_min} * CP_{anox\_ox} - k_{O2\_U\_max}}{0.5 * (k_{O2\_U\_min} + k_{O2\_U\_max}) * (CP_{anox\_ox} - 1)} \quad [S14]$$

where $CP_{anox\_ox} = CP_{anoxic}/CP_{oxic}$ is the ratio of organic carbon to total phosphorus burial under anoxic conditions to that under oxic conditions. $sharpness = 1$ for the "sharp switch" case ($k_{O2\_U\_min} = k_{O2\_U\_max}$, so all marine burial is in the same redox environment), $sharpness = 0$ for the neutrally-stable case, and $sharpness < 0$ for globally stable cases (with non-linear amplification due to redox sensitivity of phosphorus burial, but insufficient to result in intrinsic instability).

Intermediate complexity ocean biogeochemical model description

The more realistic ocean biogeochemical model used to discuss the paleogeographic controls on the system stability is based on the 79-box intermediate-complexity representation of the global physical circulation processes from Romaniello (78), with additional representation of ocean shelves and margins, and explicit water-column biogeochemical processes including (1) single nutrient-limited restoring-based parameterisation of biological export production, (2) a parameterisation of the biological pump and remineralization of sinking organic matter with corresponding oxygen consumption, (3) burial fluxes determined by a burial efficiency parameterisation including oxygen dependence on phosphorus burial.

The ocean model employs two tracers for phosphorus and oxygen. Global marine burial fluxes of phosphorus $F_{P\_b}(O, P)$ and organic carbon $F_{Corg\_b}(O, P)$ are tabulated over a grid of atmospheric oxygen O and total marine phosphorus P by time-integrating the ocean-only model to a steady-state for each point in the O, P grid, with a restoring flux applied to maintain the prescribed total marine phosphorus P.

Oceanic transport fluxes and circulation. A schematic of the model geometry and circulation is shown in Fig S2

The time evolution of ocean tracers is given by the conservation equation:

$$\frac{dC}{dt} = \frac{dC}{dt}\Big|_{advection} + \frac{dC}{dt}\Big|_{diffusion} + SMS(C) \qquad [S15]$$

where C is the per-box tracer concentration ($\mathrm{mol\,m^{-3}}$), and the term SMS(C) ($\mathrm{mol\,m^{-3}\,yr^{-1}}$) represents biogeochemical sources minus sinks (87).

The global ocean is represented by the model of Romaniello and Derry (2010) (78), with two columns for the high-latitude ocean and the low-latitude gyres, and an additional column representing global coastal upwelling. We summarize here the key aspects of the advection and eddy diffusion representation of the ocean circulation, for details please see the original paper. The advection fluxes represent: Antarctic bottom water flux (AABW=17 Sv, where 1 Sv = $10^6\,\mathrm{m^3\,s^{-1}}$), Antarctic Intermediate Water flux (AAIW = 12 Sv), North Atlantic Deep Water (NADW = 17 Sv), coastal upwelling flux (18 Sv), and especially, a non-local mixing flux to represent the ventilation of the gyre thermocline along outcropping isopycnals (220 Sv). Vertical eddy diffusion fluxes are characterized by a depth-dependent vertical eddy diffusion coefficient increasing from $\kappa_z \approx 10^{-5}\,\mathrm{m^2\,s^{-1}}$ in the thermocline to $\approx 10^{-4}\,\mathrm{m^2\,s^{-1}}$ in the deep ocean, with higher values from $10^{-2}\,\mathrm{m^2\,s^{-1}}$ to $10^{-3}\,\mathrm{m^2\,s^{-1}}$ used to account for the high rate of mixing in the high-latitude region. Isopycnal eddy diffusion fluxes corresponding to $\kappa_h \approx 1000\,\mathrm{m^2\,s^{-1}}$ share the pathways of advective fluxes between laterally adjacent boxes.

To provide a more detailed and flexible representation of ocean shelves and margins, the hypsometry is modified so that the area belonging to shelves (depth < 200m) are removed from Gyre and Hlat columns of the Romaniello and Derry (2010) (78) model, and a configurable catalog of shelves added. Each shelf is represented by two cells (each 75m depth for a shelf depth of 150m), where the lower cell has an exchange flux with a cell or pair of cells from the gyre column to represent the water exchange between open seas and shelves (with exchange timescale $\approx 3\,\mathrm{yr}$), and a vertical water exchange within the shelf (timescale 0.5 yr) representing shelf vertical mixing. The ocean depth of the shelf-ocean exchange flux varies across the catalog of 21 shelves (see Fig S2), providing a range of shelf nutrient levels and hence oxygen demand. The shelf areas are then prescribed to represent the effect of different paleogeographies.

Air-sea exchange. Air-sea exchange of oxygen is represented using a piston-velocity formulation, where the air-sea oxygen flux into surface cell i is given by:

$$f_{AirseaO\,i} = k_w\, area_i\, (pO_2\, H_O(T_i) - O_{conc\,i}) \qquad [S16]$$

where pO_2 is the (prescribed) partial pressure of atmospheric oxygen, $O_{conc\,i}$ is the oxygen concentration in cell i, $k_w = 4.8\,\mathrm{m\,d^{-1}}$ is a (fixed) piston velocity, $area_i$ is the surface area of cell i, T_i is the temperature of cell i and $H_O(T_i)$ is the temperature-dependent oxygen solubility coefficient (87, 88).

Phosphorus-dependent export productivity. Biological productivity is represented by restoring the surface concentration of a single limiting nutrient (phosphorus) to a prescribed value with the restoring flux exported as particulate organic matter. The per-surface-cell export production ($\mathrm{mol\,yr^{-1}}$) is then given by:

$$f_{ExportP\,i} = (P_{conc\,i} - expect\_P_{conc\,i})\, v_i / t_{restore} \qquad [S17]$$

where $P_{conc\,i}$ is the tracer concentration, $expect\_P_{conc\,i}$ is the prescribed concentration to restore to, v_i is the volume (m^3) of surface cell i, and $t_{restore} = 0.1\,\mathrm{yr}$ is the restoring timescale. We set $expect\_P_{conc\,i} = k_{P\,i} P_{mean}$ where P_{mean} is the current mean ocean phosphorus concentration and $k_{P\,i}$ is a per-surface-cell constant chosen to approximate the modern ocean: $k_{P\,i} = 0$ for the gyre column, 1.0 for the high-latitude column, 0.4 for the upwelling column, and 0.0 for the shelf surface cells. We then use the Redfield ratios of $Corg/PO_4$ (106.0) and N/PO_4 (16.0) to define the composition of exported particulate organic matter.

Depth-dependent particle flux. Vertical particle sinking is represented as instantaneous vertical transport with a modified formulation from Martin's power-law decay (89) of export flux with depth (after (78)):

$$f_{output\,i} = f_{input\,i} * (z_{upper}/z_{lower})^{0.858} \quad \text{[S18]}$$

where $f_{input\,i}$ is the input particulate flux into the top of cell i, $f_{output\,i}$ is the flux reaching the base of the cell, and z_{upper} and z_{lower} are the heights of the upper and lower cell surfaces. The particle flux $f_{input\,i} - f_{output\,i}$ is then remineralized, returning nutrient to the water column P tracer and consuming oxygen tracer. The model hypsometry is then used to calculate the flux $f_{SedFrac\,i}$ intercepted by the sediment surface, with the remainder providing the input flux to the cell below:

$$f_{SedFrac\,i} = f_{output\,i} * (area_{floor\,i}/area_i) \quad \text{[S19]}$$

where the $area_{floor\,i}$ and $area_i$ are the area belonging to the sediment surface and the area of the top layer in cell i, respectively.

Depth-dependent burial efficiency. Burial fluxes are calculated from the oceanfloor particulate flux $f_{SedFrac\,i}$, multiplied by a burial efficiency function. This follows the empirical parameterization used by Ozaki (90) modified by a global parameter k_{BEorg} that is adjusted to provide a global marine organic carbon burial flux of $4.5 \times 10^{12}\,\mathrm{mol\,yr^{-1}}$.

The burial efficiency of sedimentary organic carbon $BEorg$ is parameterized as a function of sedimentation rate (91) ($SedR$, in $\mathrm{cm\,yr^{-1}}$):

$$BEorg = k_{BEorg}\,(100 * SedR)^{0.4}/2.1 \quad \text{[S20]}$$

where the sedimentation rate is parameterized as a function of water depth (92) (z, in m)

$$SedR = 10^{-2} * 10^{\mathrm{erfcinv}(-z/2700)-2.1} \quad \text{[S21]}$$

Phosphorus burial is calculated from the organic carbon burial in each oceanfloor cell using an oxygen-dependent burial ratio $CP_{burial\,i}$, where

$$CP_{burial\,i} = \begin{cases} CP_{anoxic} & O_{conc\,i} < 5\,\mu\mathrm{M} \\ CP_{oxic} & O_{conc\,i} > 6\,\mu\mathrm{M} \end{cases} \quad \text{[S22]}$$

and is linearly interpolated for oxygen concentrations between these values.

Summary of sensitivity tests and additional results figures

The dynamics and stability of the 2D phosphorus (P) oxygen (O) and 3D phosphorus (P) oxygen (O) carbon (A) systems are determined by the geometry of the nullcline surfaces or lines, their intersections, and the location of folds in the critical manifold (P nullcline). The purpose of the sensitivity tests is to find the main controls (biogeochemical processes, and critical model parameters) on the shape of each nullcline surface and on fold locations, and to illustrate the effect on dynamics. We provide a summary of these tests as well additional results below. All the model configurations and corresponding parameterisations used are listed in SI Table 4, and the results are discussed in the main text and/or figure captions.

S5 P-O 2D system: "Hysteresis bifurcation" of the critical manifold in the phosphorus-oxygen model.

S6 P-O 2D system: effect of oxygen nullcline location on limit cycle oscillation and oxic/anoxic "waveform".

S7 P-O 2D system: excitation of an OAE in the phosphorus-oxygen model by instantaneous phosphorus input and rate-dependent increase in phosphorus weathering.

S8 P-O-A 3D system: baseline case POA 12 used for the main paper (Fig. 5). All the sensitivity tests below modify one parameterisation relative to POA 12.

S9 P-O-A 3D system: sensitivity test for P weathering scaling with different combinations of silicate, carbonate, and organic carbon oxidative weathering, temperature sensitivity of silicate weathering.

S10 P-O-A 3D system: sensitivity test for effect of a "low" organic cycle size with parameters from (77).

S11 P-O-A 3D system: sensitivity test for effect of a "high" degassing flux with parameters from (77).

S12 P-O-A 3D system: testing sensitivity to "sharpness" of fold in critical manifold and to local oxygen dependence of Corg:P burial ratio.

S13 P-O-A 3D system: sensitivity test for effect of a low change in Corg:P ratio between oxic and anoxic conditions.

S14 P-O-A 3D system: excitation of an OAE event by rate-dependent increase in degassing.

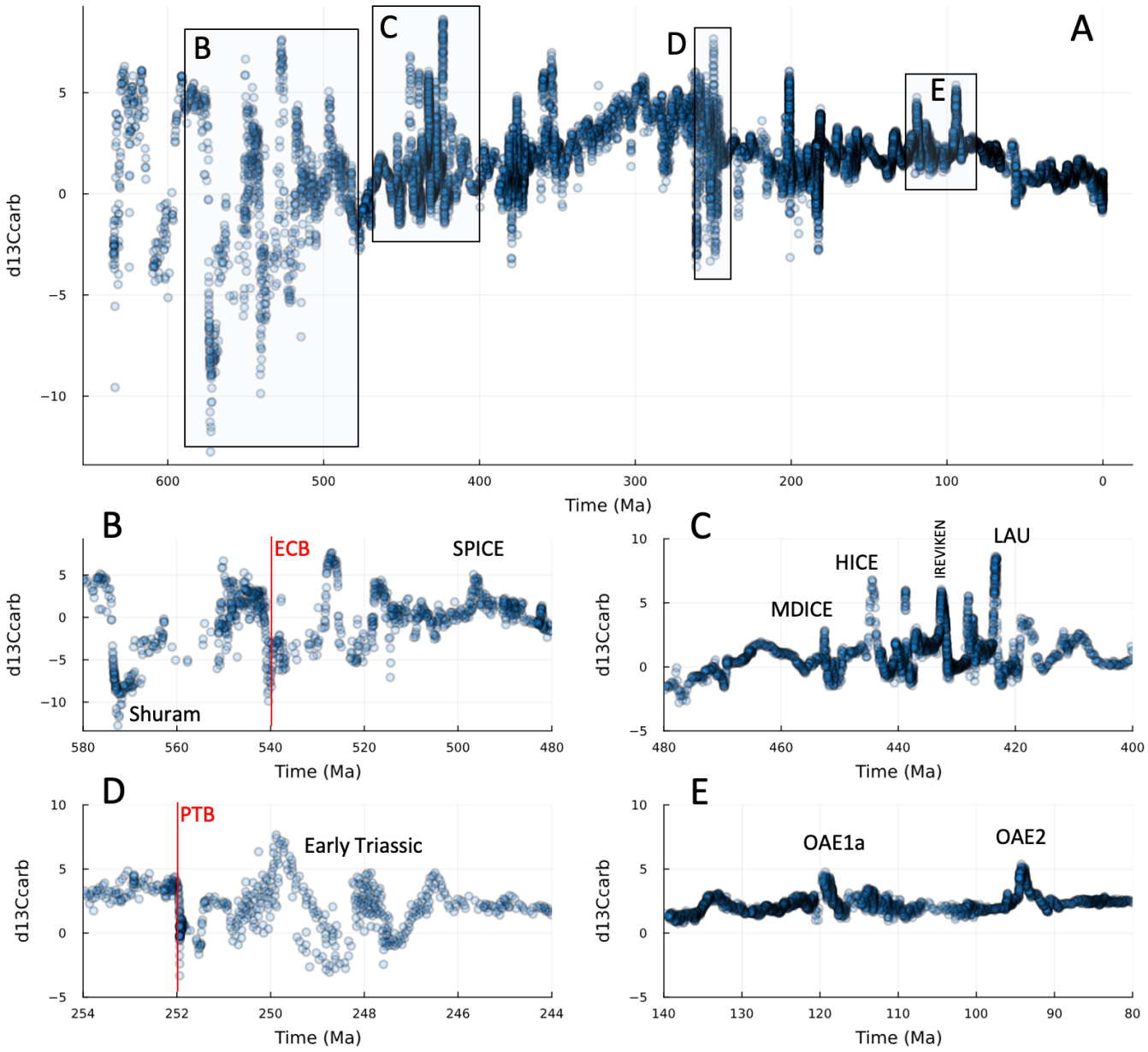

Fig. S1. The Neoproterozoic-Phanerozoic $\delta^{13}C$ record from GTS-2020 (18), with selected intervals shown on an expanded scale (after (20)). (**A**) the main panel shows the secular trend towards decreasing amplitude of excursions through the Neoproterozoic-Phanerozoic. (**B**) an expanded scale shows examples of late Ediacaran-Cambrian $\delta^{13}C$ excursions. Note that this figure does not include updates to the stratigraphy from (19) (**C**) an expanded scale shows examples of Ordovician-Silurian-early Devonian excursions. (**D**) an expanded example of end Permian-early Triassic excursions. (**E**) an expanded example of the middle Cretaceous $\delta^{13}C$ excursions representing OAE1 to OAE2.

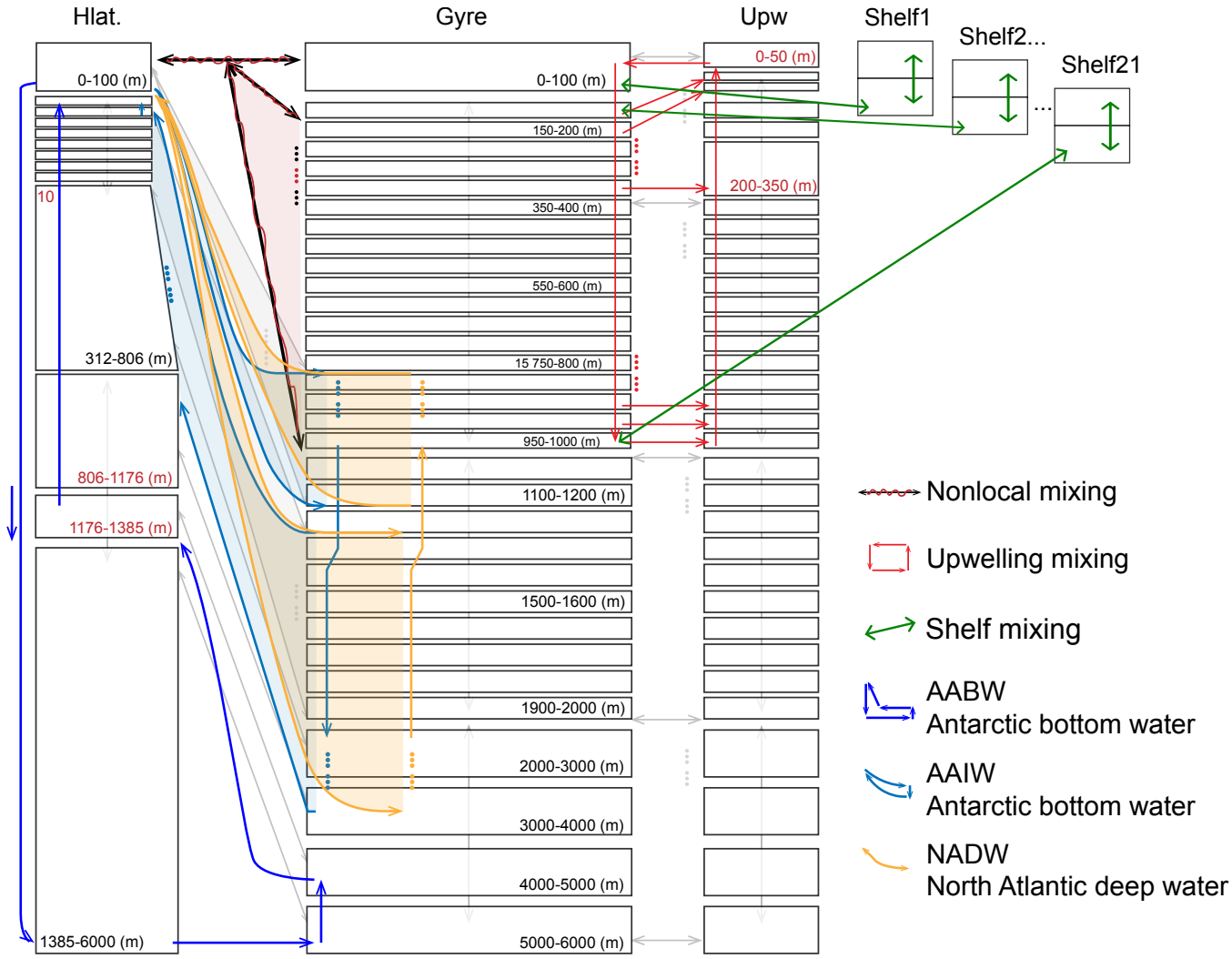

Fig. S2. Intermediate-complexity ocean model circulation. High-latitude, gyre and upwelling regions are based on Romaniello et al. (2010) model for the modern global ocean (78). Hypsometry is modified to exclude regions shallower than 200m (ie ocean shelves), and a configurable catalog of shelves is added each represented by two boxes with vertical mixing and an exchange flux connecting the lower box to one or two boxes in the global "gyre" column.

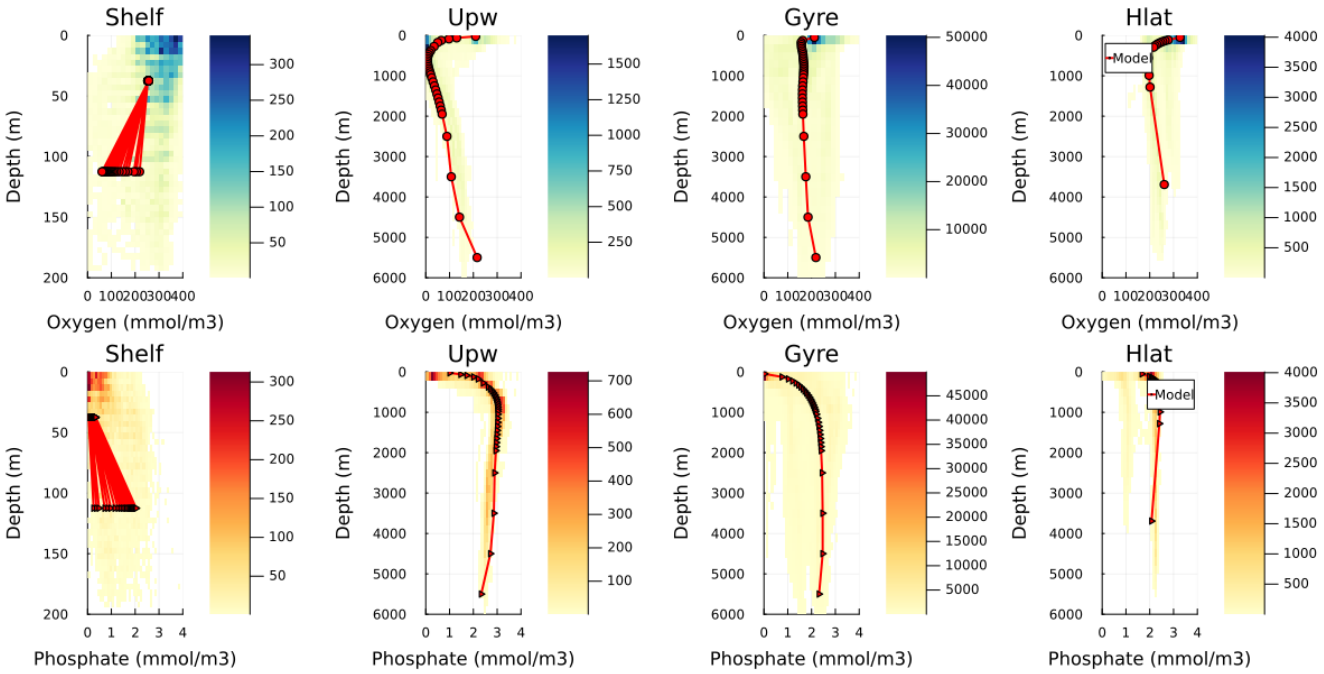

Fig. S3. Simulated oxygen and phosphate concentration for four model regions, and the comparison with the modern ocean profiles from GLODAP v2.2020 (93)

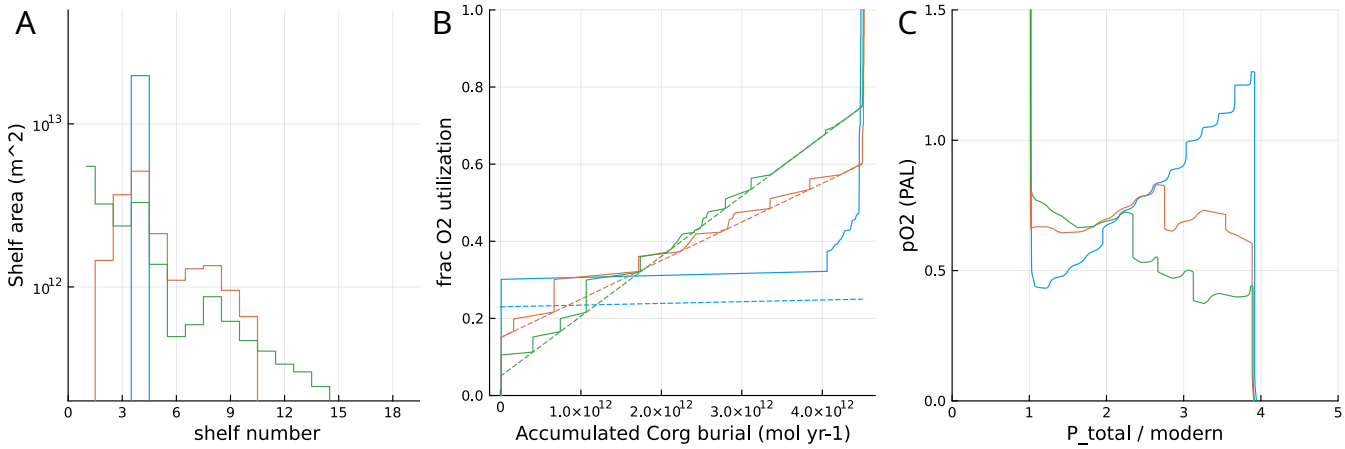

Fig. S4. Demonstration of shelf paleogeographic controls on burial redox environment and stability using an intermediate-complexity ocean model (expanded version of Fig. 2 *C2* in main paper). Shelf area (**A**) is adjusted to approximate the three idealized scenarios for the distribution (**B**) of organic carbon burial across different shelf nutrient and hence redox environments from main paper Fig. 3. (**C**) phosphorus-oxygen phase plane showing corresponding contours of constant phosphorus burial, equivalent to the critical manifold ($dP/dt = 0$). Blue lines: "sharp switch" regime, with organic carbon and phosphorus burial concentrated on a single shelf environment; red lines, neutrally stable regime; green lines: globally stable regime with burial distributed over a wide range of redox environments

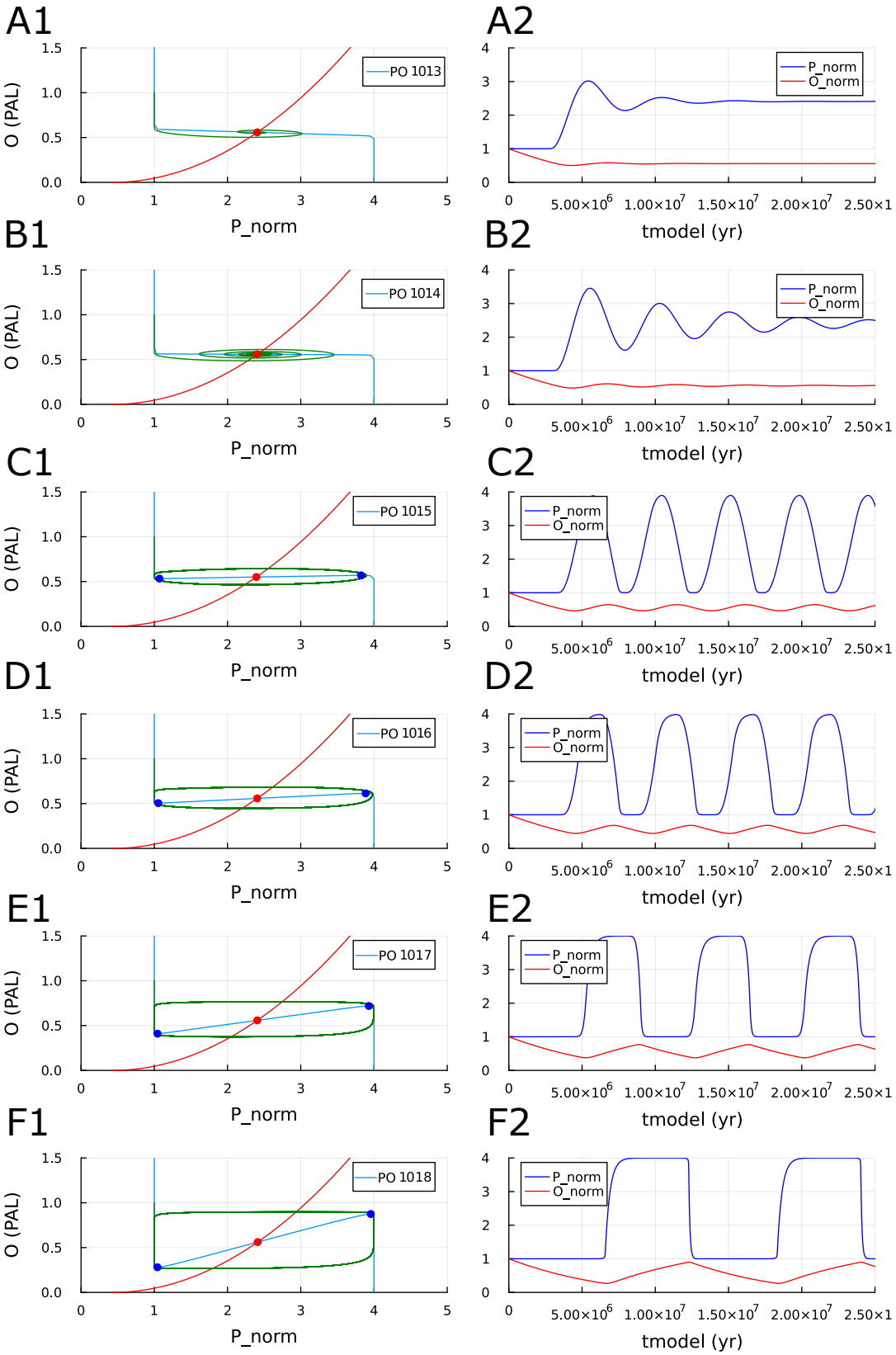

Fig. S5. "Hysteresis bifurcation" of the critical manifold in the phosphorus-oxygen model from globally stable (top panels) to "sharp switch" (bottom panels), controlled in the idealized column model by organic carbon burial distribution. Note that timescale separation breaks down near the neutrally stable limit (cases S40, S41), and hence the shortest oscillation period is still much longer than the phosphorus timescale. The exactly neutrally-stable case S40 shows a damped spiral during the approach to equilibrium, with an oscillation period $\approx (\tau_P \tau_O)^{0.5} \approx 4.7\mathrm{My}$ (the geometric mean of the phosphorus timescale τ_P and oxygen timescale τ_O), decaying on a timescale $\approx \tau_O$ (see derivation in SI Appendix). The near-neutral unstable case S41 has a similar oscillation period, and illustrates breakdown of timescale separation with no sharp jumps in P. Most of the duration of a limit cycle oscillation (cases S29, S28, S26) is spent during the increase and decrease of oxygen on a slow manifold near to the critical manifold, with fast jumps at near constant oxygen once a fold is reached, hence the sharp switch case S26 has the largest oxygen excursion and longest-period oscillation $\approx 12\mathrm{My} \approx \tau_O$.

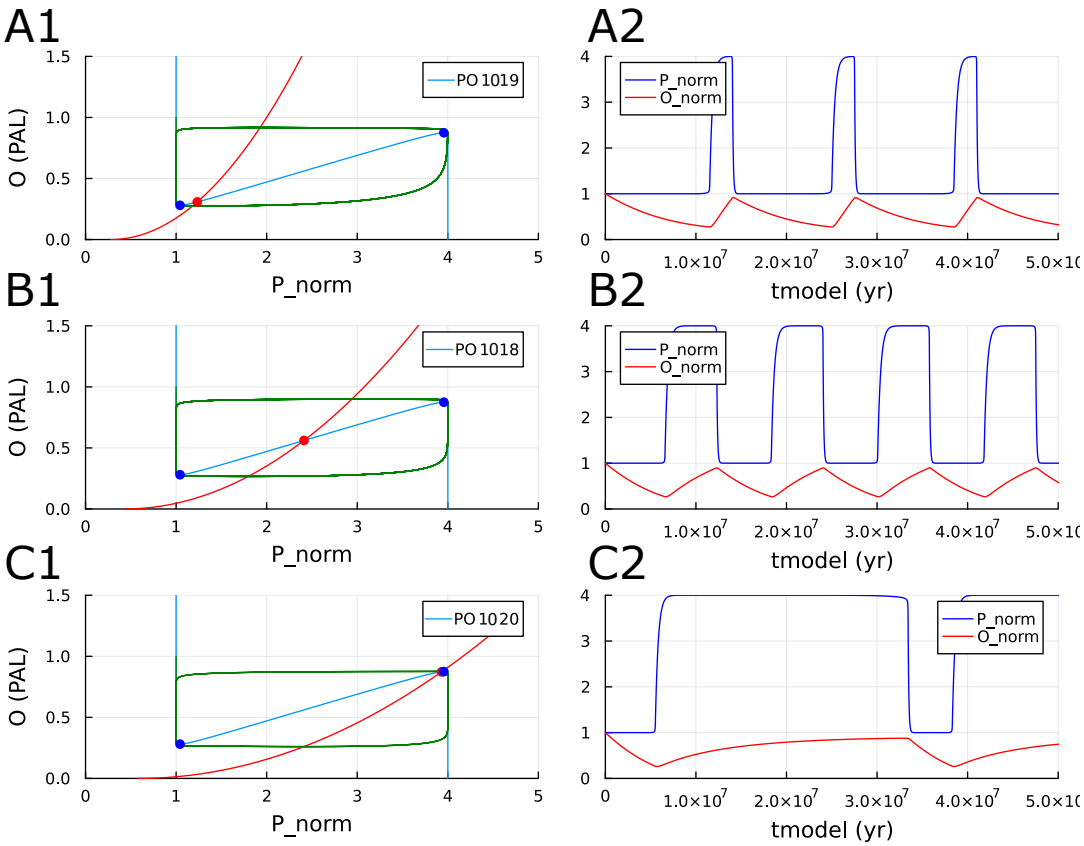

Fig. S6. Effect of oxygen nullcline location on limit cycle oscillation and oxic/anoxic "waveform" in the phosphorus-oxygen model. Marginally unstable cases where the equilibrium point (where the oxygen nullcline crosses the repelling part of the critical manifold) is close to a fold have longer oscillation period with most of the time spent near the equilibrium point where the rate of change of oxygen is slow, whereas the event time (the excursion around the limit cycle) remains approximately constant.

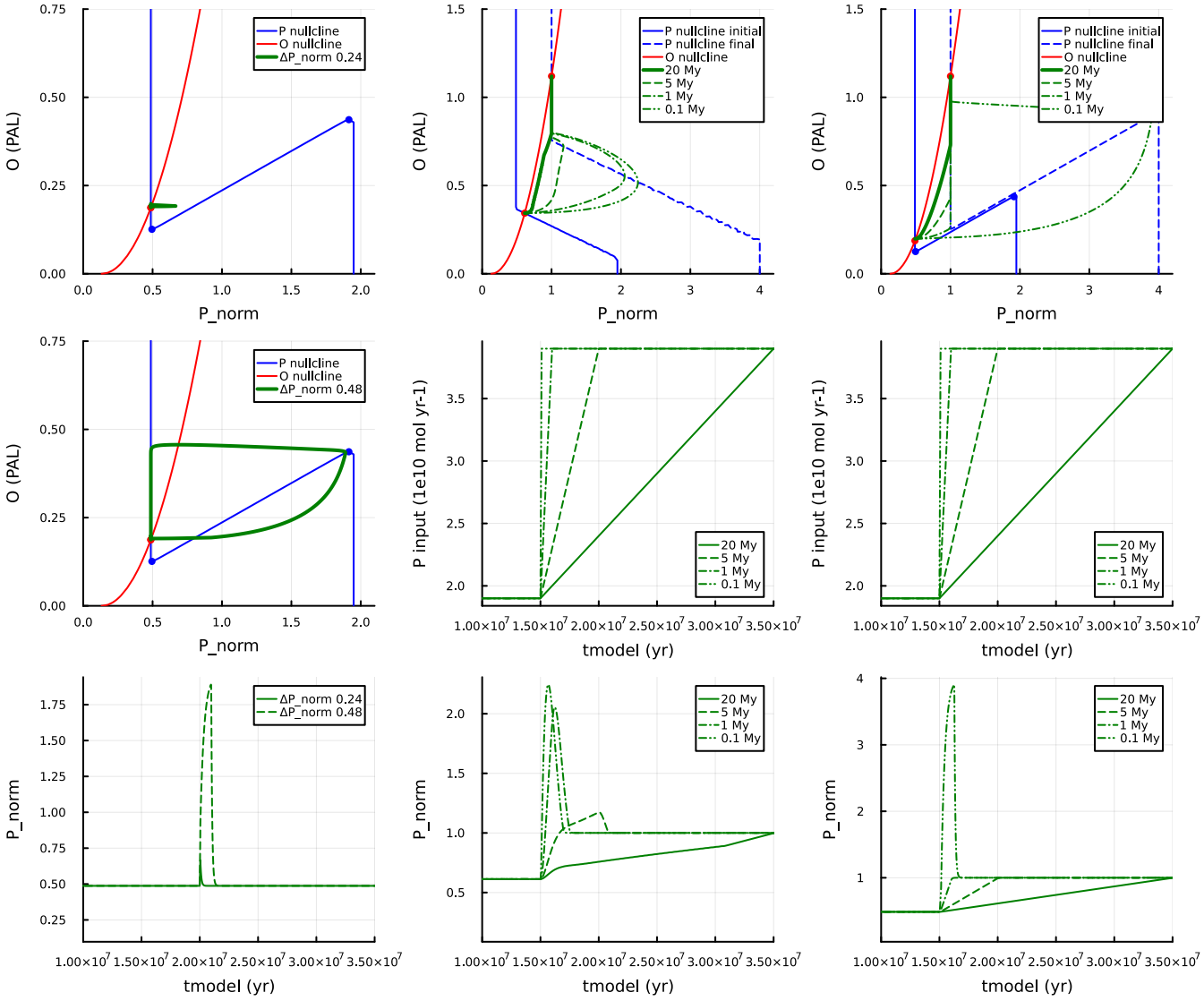

Fig. S7. Excitation and rate-dependent forcing of an OAE in the phosphorus-oxygen model by increases in phosphorus weathering input (expanded version of main paper Fig. 6). Left column: Excitation of an OAE by a small short-duration pulse in P weathering input. The steady state is oxic and near a fold. A small phosphorus pulse generates a small (effectively instantaneous) perturbation to the state variable P, and leads to a small response (top left panel). A slightly larger perturbation moves the system outside of the domain of stability bounded by the repelling branch of the critical manifold, resulting in a trip around the limit cycle (middle left panel). This scenario can also be interpreted as demonstrating the response to instantaneous movement of the nullclines in response to forcing of parameters. Middle column: Rate-dependent response of a globally-stable system to a linear ramping of phosphorus weathering input from 1.9 to $3.9 \times 10^{10} \mathrm{mol yr}^{-1}$ at a finite rate. The solid and dashed blue lines show the critical manifold for the initial and final phosphorus weathering input fluxes. If the rate of increase is slow than or comparable to the oxygen timescale the system approximately tracks the oxygen nullcline during the adjustment process and the ocean remains oxic. A faster rate results in a large increase in P amplified by the development of anoxia, before oxygen can rise. Right column: As middle column, for a system in the excitable regime with a marginally stable oxic initial state close to a fold. Fast ramping results in a limit cycle excursion, as the oxygen response time is too slow to allow the trajectory to intersect the fold in the critical manifold.

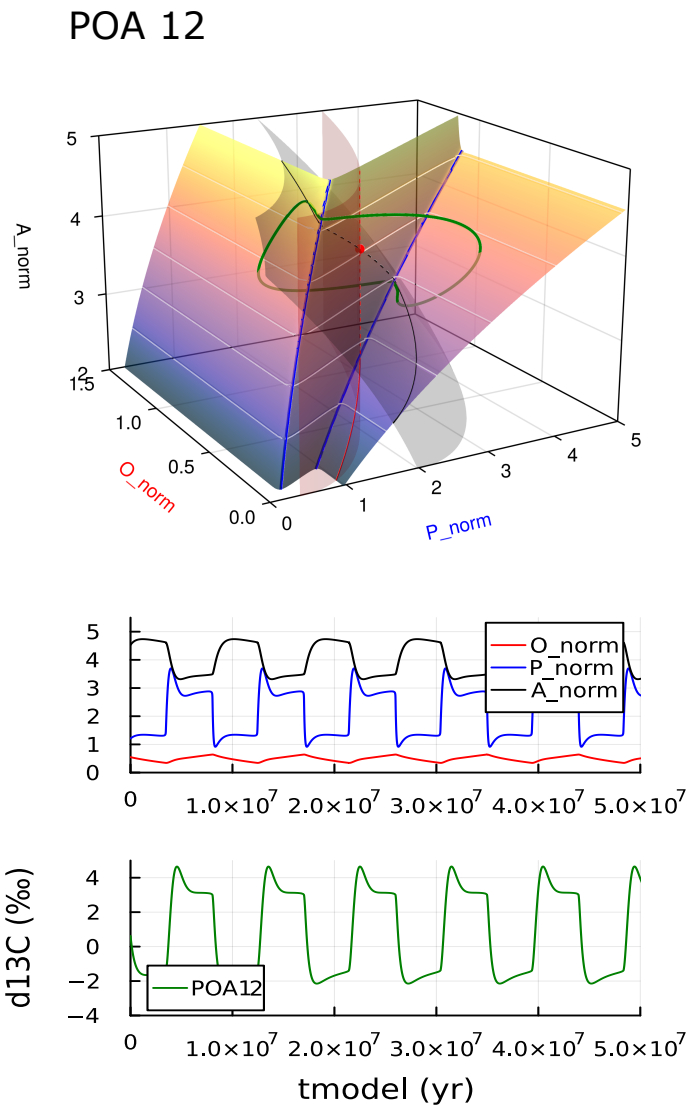

Fig. S8. Baseline configuration for POA model sensitivity tests. POA 12, as main paper Fig. 5, showing limit cycle oscillation with period 8.8 My. See Table S4 for details of configuration: all phosphorus weathering is assumed to scale with silicate weathering, default temperature sensitivity of silicate weathering, low CO2 degassing, "large" organic carbon cycle size, "sharp switch" ocean P burial, Corg:P burial ratio varies by a factor of 4 between oxic and anoxic conditions

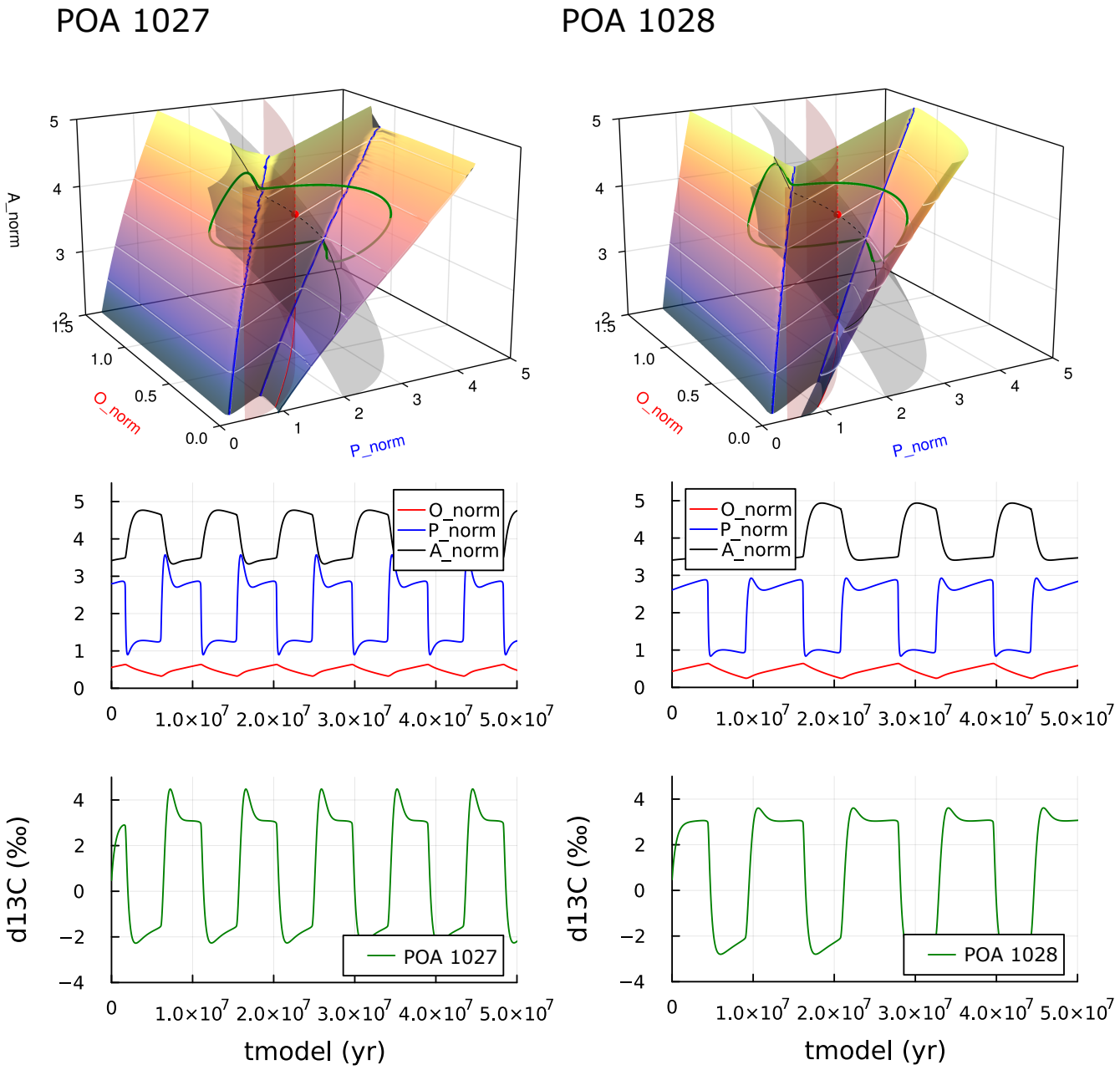

Fig. S9. POA model sensitivity to weathering parameters. POA 1027: phosphorus weathering scales with the combination of silicate (0.8), carbonate (0.14) and organic carbon oxidative weathering (0.06) used by the COPSE reloaded model (77). This is silicate-weathering dominated hence close to the baseline configuration (Figure S8). POA 1028 phosphorus weathering scales with the combination of silicate (0.2), carbonate (0.4) and organic carbon oxidative weathering (0.4) used by the COPSE model (33). As the oxidative weathering fraction 0.4 of phosphorus weathering scales $\propto O^{0.5}$ this introduces an oxygen-dependence on the P critical manifold with reduced phosphorus weathering input at low oxygen.

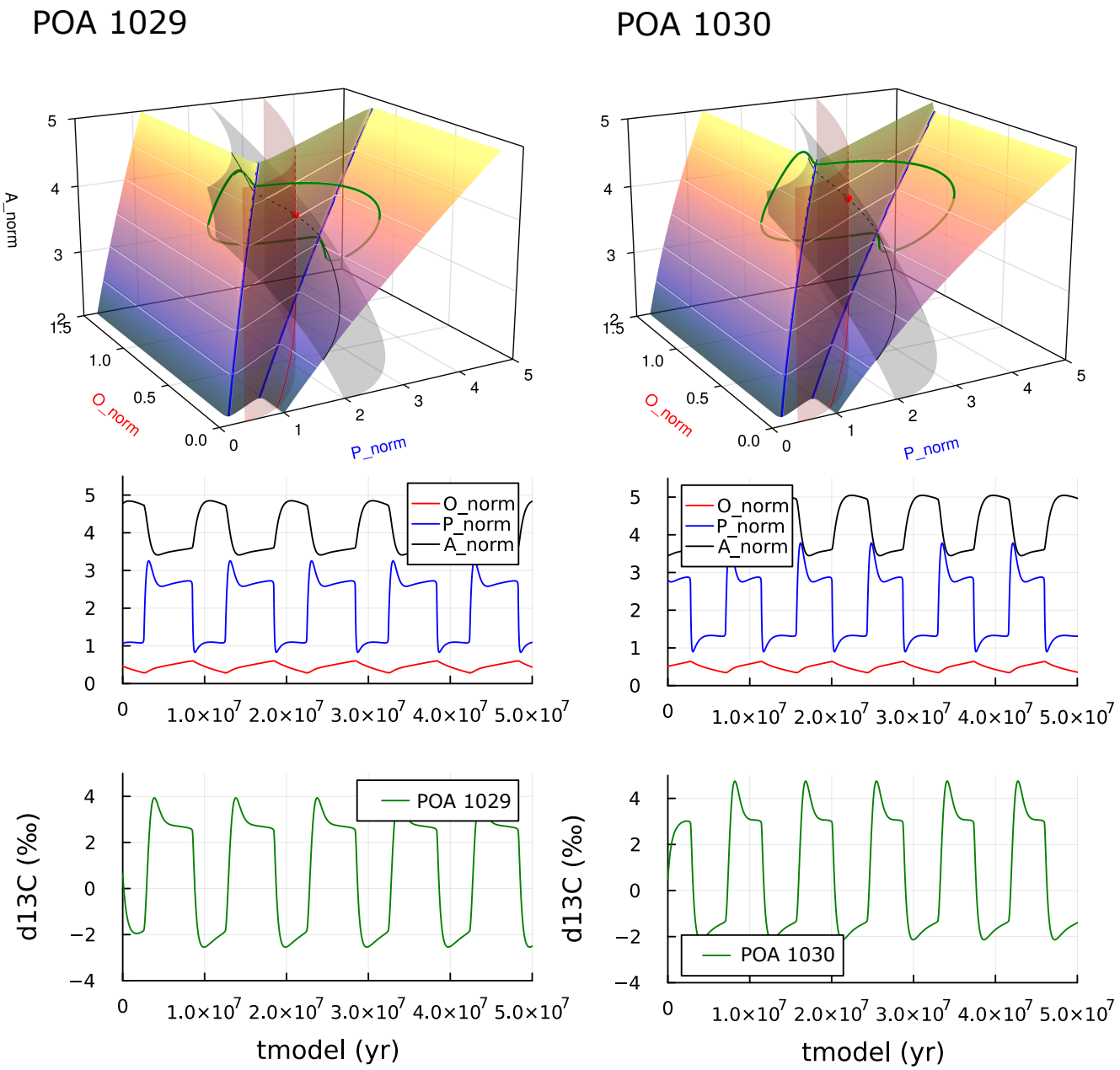

Fig. S9. POA model sensitivity to weathering parameters (continued). POA 1029: All phosphorus weathering assumed to scale with silicate weathering, with modified temperature sensitivity of silicate weathering relative to the baseline (Figure S8). POA 1030 all phosphorus weathering assumed to scale with carbonate weathering. These tests demonstrate that changes to carbonate and silicate weathering parameterisations within the range considered by the COPSE (33) and COPSE reloaded (77) do not have a significant direct effect on the limit cycle behaviour.

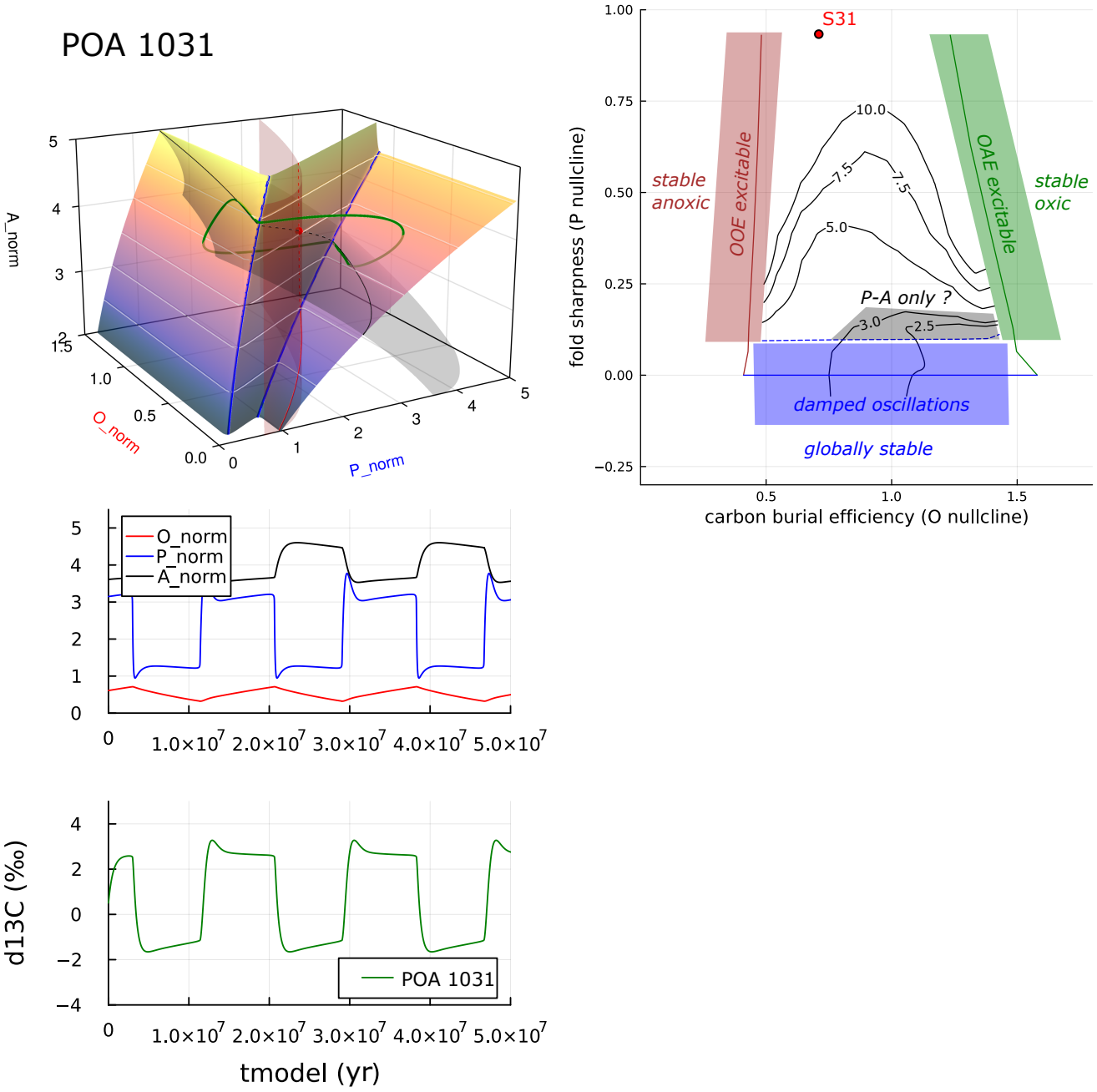

Fig. S10. POA model sensitivity to organic carbon cycle size. POA 1031 "low" organic carbon cycle size with model parameters from COPSE reloaded (77) corresponding to a modern marine organic carbon burial of $2.5 \times 10^{12} \mathrm{mol\ yr}^{-1}$, compared to the baseline configuration $4.5 \times 10^{12} \mathrm{mol\ yr}^{-1}$ from COPSE (33) (left panels: compare to Figure S8; right panel: compare to stability diagram Fig. 10 in main text). This has three effects: (i) organic carbon burial is now less significant relative to degassing and silicate weathering, resulting in a "flattening" of the A nullcline hence a smaller excursion in A and a larger excursion in O; (ii) an approximate doubling of the oscillation period to 17.4 My. hence a smaller magnitude of change in A_{norm} axis and a more P-O dominated system; (iii) the region in the stability diagram with faster limit cycle oscillation period (P-A dominated system, grey shading) is reduced (compared to that in the stability diagram Fig.6 in the main text).

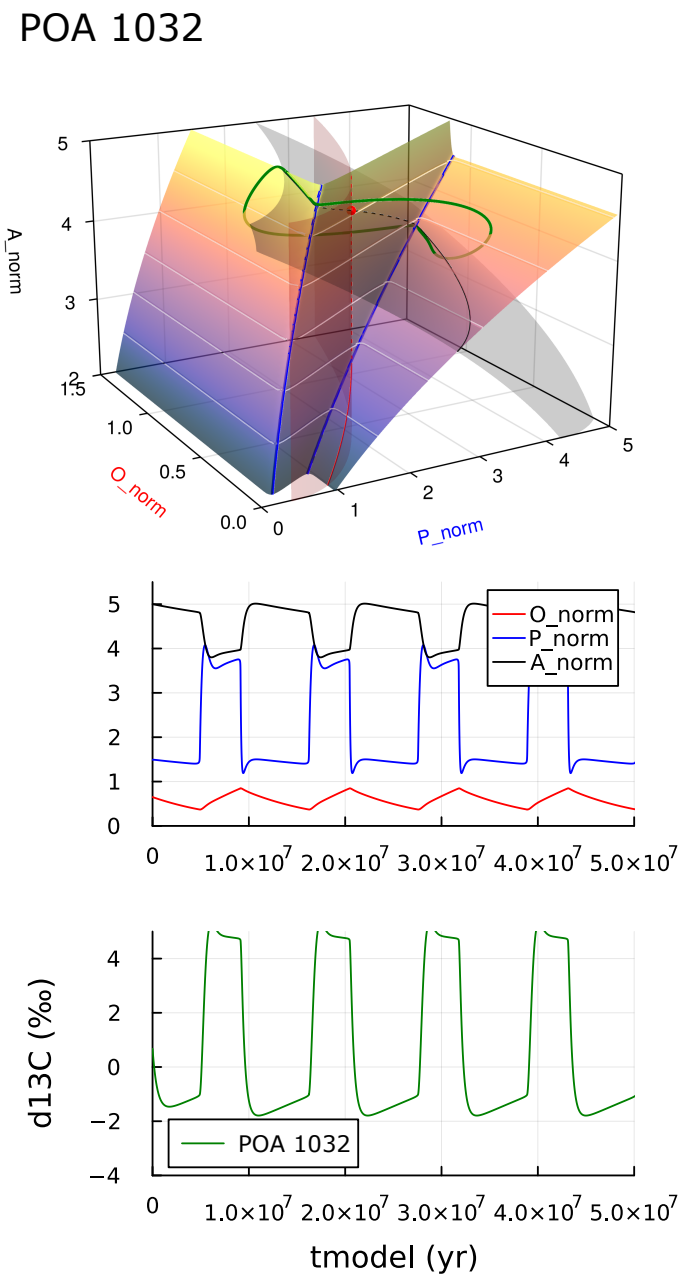

Fig. S11. POA model sensitivity to degassing. POA 1032: "high" degassing flux of $15 \times 10^{12} \mathrm{mol\ yr}^{-1}$ from COPSE reloaded (with corresponding increase in silicate weatherability and decrease in carbonate weathering), compared to the baseline configuration of $6.65 \times 10^{12} \mathrm{mol\ yr}^{-1}$ from COPSE (33) (Figure S8). Organic carbon burial is now less significant relative to degassing and silicate weathering, resulting in a "flattening" of the A nullcline hence a smaller excursion in A and a larger excursion in O (cf Fig. S10, oscillation period is increased to 11.1 My.

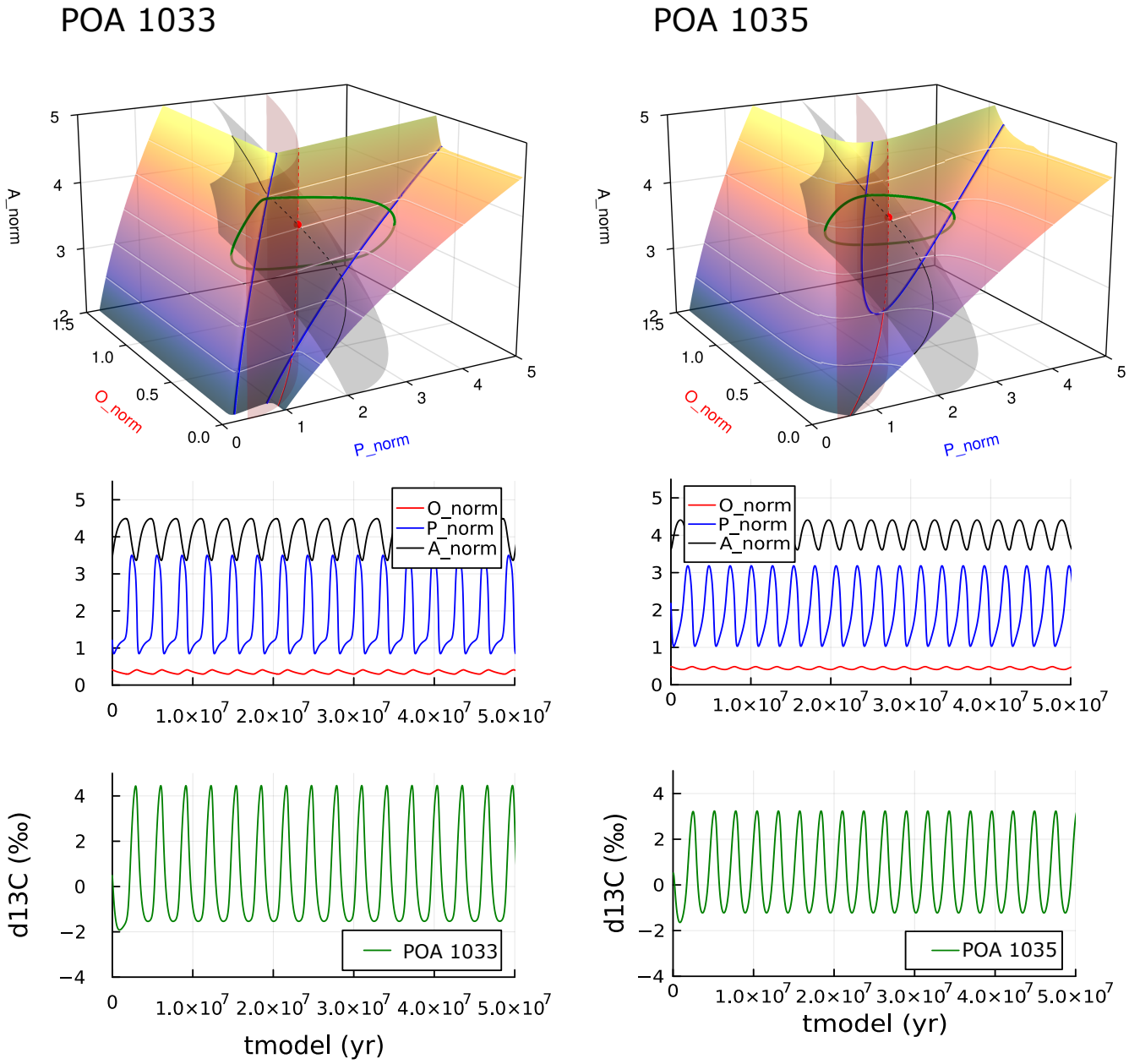

Fig. S12. POA model sensitivity to "sharpness" of fold in critical manifold and to local oxygen dependence of Corg:P burial ratio. POA33: Effect of a "less folded" critical manifold (intermediate between the "sharp switch" used in the baseline configuration (Figure S8) and "neutrally stable" cases (not shown). The limit cycle now reaches the fold points before the dA/dt=0 nullcline, hence there are no slow segments on the oxygen timescale, resulting in a faster limit cycle with oscillation period of 3.1 My. POA 35: sensitivity to local oxygen dependence of Corg:P burial ratio (Eq. S11). The parameterisation of the oceanfloor redox environment is the same as that of the baseline case (POA 12, Fig. S8, a "sharp switch" with all marine burial sharing the same redox environment). Here the k_{anox} parameter is reduced to 10, so that the redox-dependent change in local Corg:P burial ratio now occurs over a larger range in oceanfloor oxygen concentration of 0.1 in normalized units or $\approx \pm 30\ \mu\mathrm{M}$, compared to the baseline value of $k_{anox} = 100$ (oxygen range $\approx \pm 3\ \mu\mathrm{M}$). This has a qualitatively similar effect on the fold positions to that of the change in parameterisation of the global oceanfloor redox environment shown in case POA 33, resulting in a faster limit cycle with oscillation period of 2.6 My. The effect of the more gradual local transition in Corg:P burial ratio with oceanfloor oxygen concentration is proportionately larger at lower oxygen levels, and with the parameters used here the two fold lines intersect in the low P_{norm} and low O_{norm} part of the phase space.

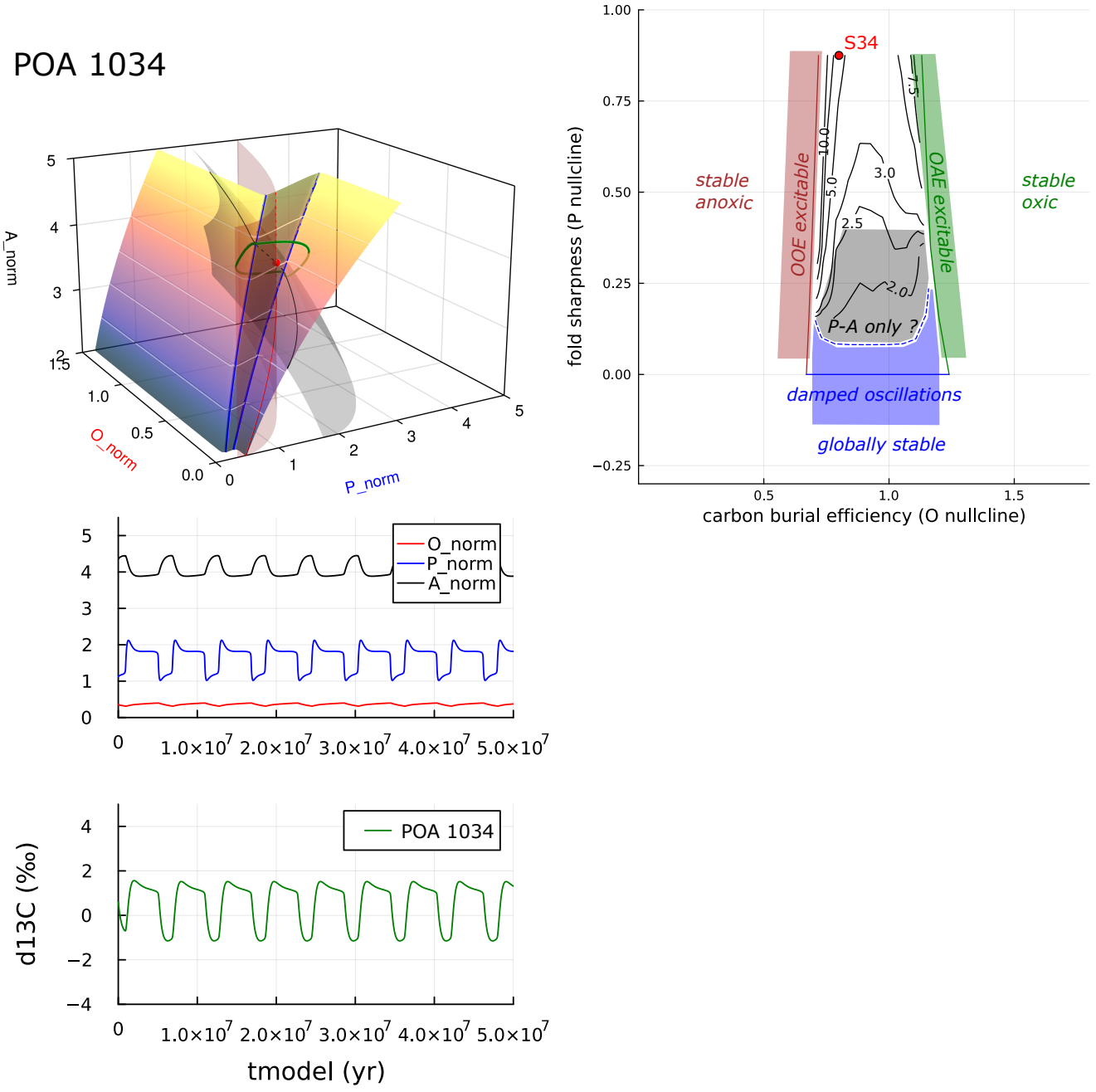

Fig. S13. POA model sensitivity to magnitude of oxic-anoxic Corg:P burial ratio change. POA 1034: Effect of a lower range in Corg:P burial ratio between oxic and anoxic conditions (a factor of 2, compared to a factor of 4 used in the baseline case (left panels: compare to Figure S8; right panel: compare to stability diagram Fig. 10 in main text). This results in corresponding reductions in the range in P between oxic and anoxic conditions, the range in organic carbon burial, and hence in the $\delta^{13}C$ excursion. Oscillation period is reduced to approx 2/3 of that of the baseline case.

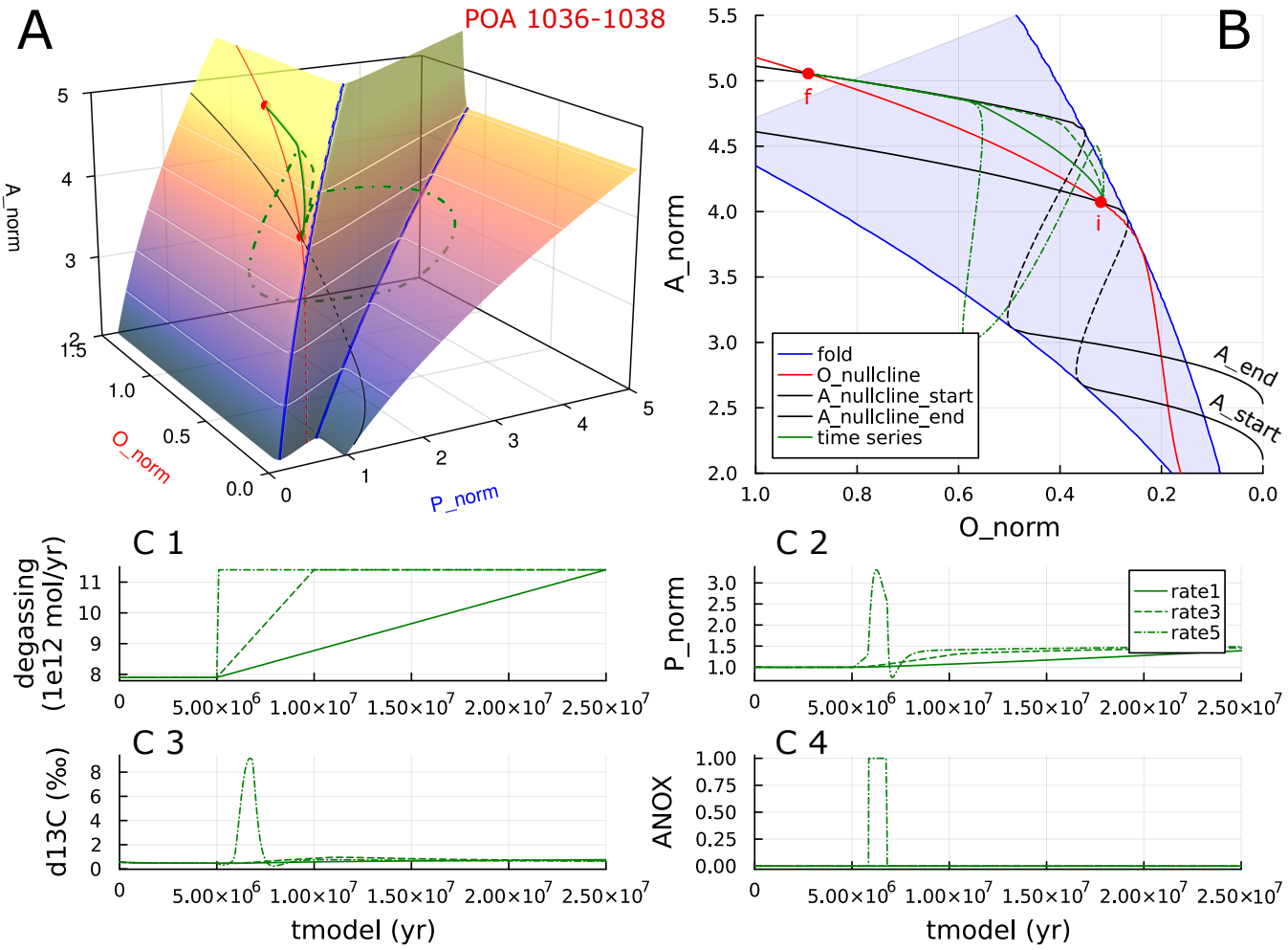

Fig. S14. Excitation of an OAE event by a rate-dependent increase in degassing from 6.65×10^{12} to 10.15×10^{12} mol yr^{-1}. A slow linear increase in degassing forcing relative to the oxygen timescale (solid and dashed green lines, increase over 5, 20 My) results in the system remaining oxic, with the adjustment process from initial steady-state i to final steady state f approximately following the dO/dt=0 nullcline and remaining in the attracting oxic sheet of the critical manifold. A fast increase in degassing (dash-dot green line) results in the initial adjustment trajectory at approximately constant oxygen reaching the fold, resulting in a limit cycle and OAE. With the parameters shown, the limiting rate (approximately the green dashed line) corresponds to a timescale of approximately 5 My.

Table S1. Atmosphere, climate and land model equations

Variable/Process	Equation	Units	References/Notes
Key variables			
Atmosphere $p\mathrm{CO_2}$	$p\mathrm{CO_2} = (A/A_0)^2$	PAL	COPSE (33, 77)
Global temperature relative to $15^\circ\mathrm{C}$	$\Delta T = k_{CO2} * \ln(p\mathrm{CO_2}) - k_{SL} * (age/570\mathrm{Ma})$	K	GEOCARB (44), COPSE (77), constant $age = 600\,\mathrm{Ma}$
Pre-plant weathering $p\mathrm{CO_2}$ dependence	$f_{preplant} = k_{15} * (p\mathrm{CO_2})^{0.5}$	-	GEOCARB (44), COPSE (33, 77)
Kinetics granite temperature dependence	$f_{Tgran} = exp(k_{Tgran} * \Delta T)$	-	COPSE (77)
Kinetics basalt temperature dependence	$f_{Tbas} = exp(k_{Tbas} * \Delta T)$	-	COPSE (77)
Runoff silicate temperature dependence	$f_{runoff} = (1 + 0.038 * \Delta T)^{0.65}$	-	GEOCARB (44), COPSE (33, 77)
Runoff carbonate temperature dependence	$g_{runoff} = 1 + 0.087 * \Delta T$	-	GEOCARB (44), COPSE (33, 77)
Carbon fluxes			
Granite weathering	$granw = k_{granw} * U * a_{gran} * f_{Tgran} * f_{runoff} * f_{preplant}$	$\mathrm{mol\,C\,yr^{-}1}$	GEOCARB (44), COPSE (77)
Basalt weathering	$basw = k_{basw} * a_{bas} * f_{Tbas} * f_{runoff} * f_{preplant}$	$\mathrm{mol\,C\,yr^{-}1}$	GEOCARB (44), COPSE (77)
Silicate weathering	$silw = granw + basw$	$\mathrm{mol\,C\,yr^{-}1}$	COPSE (33, 77)
Carbonate weathering	$carbw = k_{14} * U * g_{runoff} * f_{preplant}$	$\mathrm{mol\,C\,yr^{-}1}$	GEOCARB (44), COPSE (33, 77)
Organic C oxidation	$oxidw = k_{17} * U * (O/O_0)^{0.5}$	$\mathrm{mol\,C\,yr^{-}1}$	COPSE (33, 77)
Organic C degassing	$ocdeg = k_{13} * D$	$\mathrm{mol\,C\,yr^{-}1}$	
Carbonate degassing	$ccdeg = k_{12} * D$	$\mathrm{mol\,C\,yr^{-}1}$	
Terrestrial C_{org} burial	$locb = 0$	$\mathrm{mol\,C\,yr^{-}1}$	option: constant $locb = 4.5 \times 10^{12}$ mo
Phosphorus fluxes			
Fraction of P weathering from silicate	$Psilw = k_{Psilw} * silw/(k_{granw} + k_{basw})$	$\mathrm{mol\,P\,yr^{-}1}$	COPSE (33, 77)
Fraction of P weathering from carbonate	$Pcarbw = k_{Pcarbw} * carbw/k_{14}$	$\mathrm{mol\,P\,yr^{-}1}$	COPSE (33, 77)
Fraction of P weathering from organic matter	$Poxidw = k_{Poxidw} * oxidw/k_{17}$	$\mathrm{mol\,P\,yr^{-}1}$	COPSE (33, 77)
Reactive P weathering	$phosw = k_{10} * (Psilw + Pcarbw + Poxidw)$	$\mathrm{mol\,P\,yr^{-}1}$	COPSE (33, 77)
Reactive P weathering to ocean	$psea = phosw - pland$	$\mathrm{mol\,P\,yr^{-}1}$	constant $pland = 0$

Table S2. Atmosphere, climate and land model constants

Process/Forcing	Label	Value	Units	References/notes
Model forcings				
Metamorphic and volcanic degassing	D	1.0		COPSE (33, 77)
Tectonic uplift	U	1.0		COPSE (33, 77)
Normalised granite area	a_{gran}	1.0		COPSE (77)
Normalised basalt area	a_{bas}	1.0		COPSE (77)
Model climate				
Climate sensitivity control	k_{CO2}	4.328	$^{\circ}\mathrm{C}$	GEOCARB (44), COPSE (77)
Luminosity sensitivity control	k_{SL}	7.4	$^{\circ}\mathrm{C}$	GEOCARB (44), COPSE (77)
Carbon cycle				
Total atmosphere-ocean carbon present-day value	A_0	3.193×10^{18}	mol	COPSE (33, 77)
Carbonate C degassing	k_{12}	6.65×10^{12}	mol/yr	option: 15×10^{12}mol/yr
Organic C degassing	k_{13}	1.25×10^{12}	mol/yr	COPSE (33, 77)
Carbonate weathering	k_{14}	13.35×10^{12}	mol/yr	option: 8×10^{12}mol/yr
Pre-plant weathering	k_{15}	0.15		COPSE (33, 77)
Oxidative C weathering	k_{17}	7.75×10^{12}	mol/yr	option: 3.75×10^{12}mol/yr
Temperature sensitivity of granite weathering	k_{Tgran}	0.09		option: 0.0724
Temperature sensitivity of basalt weathering	k_{Tbas}	0.09		option: 0.0608
Granite weathering	k_{granw}	4.3225×10^{12}	mol/yr	COPSE (77)
Basalt weathering	k_{basw}	2.3275×10^{12}	mol/yr	COPSE (77)
Sedimentary carbonate $\delta^{13}\mathrm{C}$	$\delta^{13}_{\mathrm{carb}}$	1.0	per mil	
Sedimentary organic carbon $\delta^{13}\mathrm{C}$	$\delta^{13}_{\mathrm{corg}}$	-26.0	per mil	
Oxygen cycle				
Total atmosphere-ocean oxygen present-day value	O_0	3.7×10^{19}	mol	COPSE (33, 77)
Phosphorus cycle				
Total ocean phosphorus present-day value	P_0	3.1×10^{15}	mol	COPSE (33, 77)
Reactive P weathering	k_{10}	39×10^{9}	mol/yr	COPSE (33, 77)
Silicates fraction of P weathering	k_{Psilw}	1.0		option: 2/12, 0.8, 0.0
Carbonates fraction of P weathering	k_{Pcarbw}	0.0		option: 5/12, 0.14, 1.0
Oxidative fraction of P weathering	k_{Poxidw}	0.0		option: 5/12, 0.06, 0.0

Table S3. ICBM Ocean model simulated global ocean particulate organic carbon budget partitioned into four regions.

	Hlat	Gyre	Upw	Shelf	Sum
Surface area ($10^{14}m^2$)	0.47 (11.5%)	3.35(81.3%)	0.10(2.5%)	0.19(4.7%)	4.12
Production export ($10^{14}mol/yr$)	0.96 (7.5%)	9.58(74.4%)	0.43(3.4%)	1.89(14.7%)	12.88
Remineralization ($10^{14}mol/yr$)	0.91 (8.3%)	9.12(82.9%)	0.42(3.8%)	0.55(5.0%)	10.99
Burial ($10^{12}mol/yr$)	0.07 (1.6%)	0.38(8.7%)	0.02(0.5%)	3.96(89.2%)	4.45

Table S4. Model parameters